New Journal of Physics
The open access journal at the forefront of physics

PAPER • OPEN ACCESS

Efficient computation of coherent multimode instabilities in lasers using a spectral approach

To cite this article: Sara Kacmoli *et al* 2023 *New J. Phys.* **25** 113030

IOP Publishing New J. Phys. 25 (2023) 113030 https://doi.org/10.1088/1367-2630/ad08f1

New Journal of Physics
The open access journal at the forefront of physics

Deutsche Physikalische Gesellschaft DPG
IOP Institute of Physics

Published in partnership with: Deutsche Physikalische Gesellschaft and the Institute of Physics

OPEN ACCESS

RECEIVED
6 July 2023

REVISED
17 October 2023

ACCEPTED FOR PUBLICATION
1 November 2023

PUBLISHED
20 November 2023

PAPER

Efficient computation of coherent multimode instabilities in lasers using a spectral approach

Sara Kacmoli[1,*], Saeed A Khan[1,*], Claire F Gmachl and Hakan E Türeci

Department of Electrical and Computer Engineering, Princeton University, Princeton, NJ 08544, United States of America
[1] These authors contributed equally to this publication.
[*] Authors to whom any correspondence should be addressed.

E-mail: skacmoli@princeton.edu and saeedk@princeton.edu

Keywords: lasers, coherent instabilities, frequency combs, spectral method

Abstract

Coherent multimode instabilities are responsible for several phenomena of recent interest in semiconductor lasers, such as the generation of frequency combs and ultrashort pulses. These techonologies have proven disruptive in optical telecommunications and spectroscopy applications. While the standard Maxwell-Bloch equations (MBEs) encompass such complex lasing phenomena, their integration is computationally expensive and offers limited analytical insight. In this paper, we demonstrate an efficient spectral approach to the simulation of multimode instabilities via a quantitative analysis of the instability of single-frequency lasing in ring lasers, referred to as the Lorenz-Haken (LH) instability or the RNGH instability in distinct parameter regimes. Our approach, referred to as CFTD, uses generally non-Hermitian Constant Flux modes to obtain projected Time Domain equations. CFTD provides excellent agreement with finite-difference integration of the MBEs across a wide range of parameters in regimes of non-stationary inversion, including frequency comb formation and spatiotemporal chaos. We also develop a modal linear stability analysis using CFTD to efficiently predict multimode instabilities in lasers. The combination of numerical accuracy, speedup, and semi-analytic insight across a variety of dynamical regimes make the CFTD approach ideal to analyze multimode instabilities in lasers, especially in more complex geometries or coupled laser arrays.

1. Introduction

Lasers are complex dynamical systems the operation of which is enabled by the interaction between the field of an often-multimode cavity and a gain medium. For a considerable part of the history of lasers, experimental efforts have been focused on improving stability, monochromaticity, power performance and beam quality. This is largely due to specific applications where these attributes are desirable, such as fiber optical telecommunication, materials processing, and precision spectroscopy. Even in such high-performance regimes, nonlinear, multimode effects emerge via mode competition and spatial hole burning, which must be understood and suppressed [1, 2] to maximize laser power and efficiency. More recently, however, rather than an undesired effect, coherent multimode lasing phenomena have been the focus of many studies [3–8]. Such phenomena include ultrashort (sub-ps) pulse formation [9, 10] useful for precision machining [11] and probing of ultrafast processes [12, 13]. Active mode locking is another example traditionally linked with the generation of ultrashort pulses [14, 15]; recent efforts have focused on achieving mode locking in lasers with fast gain recovery, such as quantum cascade lasers [16, 17]. Furthermore, soliton generation has, in recent years, proven to be a disruptive technology via passive dissipative Kerr combs [18, 19] as well as active platforms [20]. Optical frequency combs—whether or not characterized by ultrashort pulses—are also a prime example of a technology hinging on coherent instabilities that has been impactful in applications of spectroscopy [21], metrology [22, 23], optical clocks [24] and optical telecommunication [25].

In contrast to standard lasing regimes marked by stationary population inversion in the gain medium, coherent multimode instabilities present in the examples above emerge in a different regime altogether: one where the lasing medium population is no longer stationary, and undergoes *population pulsations* [26]. Important studies [27–31] clarified the role of population pulsations in some of the earliest predicted examples of such dynamics: the instabilities of single-frequency lasing in ring lasers, often classed into Lorenz-Haken (LH, or 'single-mode') and Risken-Nummedal-Graham-Haken (RNGH, or 'multi-mode') instabilities [32, 33]. Either instability is marked by additional modes beyond the primary lasing mode crossing a *second* threshold. For ring lasers in particular, gain clamping in the regime of stationary inversion precludes such a threshold for standard multi-mode lasing [34]. Instead, non-stationary inversion provides the key ingredient: *parametric* gain that coherently amplifies fluctuations of pairs of sidebands. For standard ring lasers, this second threshold was predicted to be at high pump powers, rendering experimental verification elusive [35–38]. However, in more recent years, low-threshold multimode instabilities have been investigated in ring quantum cascade lasers [39–41], as well as alternate geometries including Fabry-Pérot lasers [34, 42], and the instability mechanism at play has been subject of much work.

The development of simulation tools to capture such instabilities is thus very timely. While the semi-classical Maxwell-Bloch equations (MBEs) have provided the standard description of spatio-temporal lasing dynamics across the aforementioned single and multi-mode lasing regimes, the powerful simulation methods that have been developed to simulate MBEs are computationally expensive [43, 44], and provide only limited analytic insight into these lasing phenomena. As a result, alternative simulation methods to more efficiently analyze lasing phenomena in nonlinear dynamical regimes are highly desirable. Such schemes are also particularly relevant with increasing interest in lasers of more complex geometries or coupled laser arrays [45–49], for which simulation complexity will further increase.

In this paper, we develop and validate a spectral approach to simulating complex multimode laser instabilities to address this need. While spectral or modal approaches have been used previously to analyze laser instabilities, they typically use lossless, closed cavity modes as a basis, often constrain parameter regimes to reduce the dimensionality of the MBEs [50, 51], or consider linearized MBEs only [27, 28]. Our approach differs in these key aspects. First, our spectral basis of choice is spanned by cold modes defined by the *lossy* laser cavity: the so-called constant-flux (CF) modes of the laser [52], which satisfy a generally non-Hermitian boundary value problem with associated complex eigenvalues. Even for cavities where the internal loss dominates over loss due to openness and radiation—such as the original RNGH and LH models we compare to—the modal theory must formally be constructed using eigenmodes of a non-Hermitian operator with complex eigenvalues due to intrinsic loss. Secondly, and more importantly, we analyze the full MBEs, placing no constraints on the gain medium dynamics or the number of retained modes. This requires us to use the spectral basis to perform a spatial projection of the spatiotemporal inversion field, casting the modal theory in terms of a general *time-dependent* inversion *matrix*. This non-standard representation ultimately proves crucial to correctly capturing the dynamics of the inversion field and thus of instabilities mediated by population pulsations.

The resulting coupled-mode theory, referred to as CFTD in our earlier work [53], has previously been applied to specific situations where only brief violations of stationary inversion occur, such as synchronization. However, in this paper we test and demonstrate the utility of CFTD across a wide range of regimes in ring lasers characterized by nontrivial dynamics of the gain medium, encompassing both LH and RNGH instabilities, below, past, and far above the so-called second threshold. This spans dynamical phenomena ranging from decaying spatiotemporal oscillations around a single-mode lasing state, to stable broadband frequency combs, and even chaotic dynamics. Crucially, we provide a thorough benchmarking study of CFTD across these regimes using at least one of two standard methods: finite difference time domain (FDTD) integration of multimode lasing dynamics and a split-step Runge-Kutta method (SSRK) tailored to ring lasers. We find excellent qualitative agreement across the broad range of considered regimes, with very good *quantitative* agreement in specific regimes that we identify. Furthermore, the agreement is obtained via CFTD simulations several orders of magnitude faster than FDTD or SSRK simulations.

Finally, the CFTD approach goes beyond providing an efficient numerical tool: it also forms the foundation for a modal linear stability analysis (LSA) that we show can be used to predict multimode instabilities. The modal LSA explicitly describes the instability of *discrete* modes coupled via inversion matrix elements describing gain medium dynamics. This is in contrast to more standard perturbative approaches to ring lasers, which analyze the instability of a continuous perturbation of the spatiotemporal PDE [29, 32, 54, 55] (with notable exceptions [27, 28, 30]). Not only does the modal LSA typically agree with the spatiotemporal (ST) LSA, it can at times provide additional information. In particular, the modal LSA derived from CFTD is natively aware of the laser cavity mode spectrum, unlike the ST LSA. As a result, we find it can correctly predict the absence of instabilities in parameter regimes when a newly generated

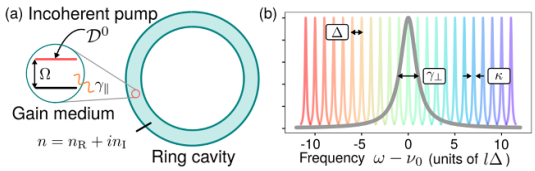

Figure 1. (a) Schematic of multimode ring laser under incoherent pumping. (b) Longitudinal mode structure of the ring cavity and gain medium response curve (grey). Here $N = 20$ cold cavity modes are depicted.

frequency does not coincide with a cavity mode, in contrast to the ST LSA. The numerical accuracy and efficiency of CFTD simulations, together with predictive capabilities provided by the modal LSA, make it ideal to study multimode instabilities in more complex, coupled laser geometries.

This paper is organized as follows. In section 2 we recount the standard description of lasing via MBEs, including their form within the slowly-varying envelope approximation typically employed in the analysis of ring laser instabilities. In section 3, we present the CFTD approach starting from the general MBEs, and obtain the set of time-dependent ordinary differential equations (ODEs) that constitute the CFTD equations. Section 4 considers the single-mode lasing regime below the multifrequency instability threshold, applied in particular to spatially non-trivial initial field distributions involving multiple spatial modes. In section 5, we consider dynamics above the threshold of the ring laser instability leading to stable frequency comb formation, as a function of laser loss parameters. In section 6 we investigate the CFTD method in a parameter space that leads to chaotic behavior, and finally in section 7 we quantify the simulation time improvement that our method has over spatiotemporal schemes.

2. MBEs for ring lasers

Lasing dynamics of a variety of lasers have been very successfully described by MBEs for the electric field inside the laser cavity $\mathcal{E}(\mathbf{r}, t)$ coupled to the polarization $\mathcal{P}(\mathbf{r}, t)$ and inversion $\mathcal{D}(\mathbf{r}, t)$ of the gain medium,

$$\nabla^2\mathcal{E} - \frac{n_c^2}{c^2}\ddot{\mathcal{E}} = \mu_0\ddot{\mathcal{P}} \tag{1a}$$

$$\dot{\mathcal{P}} = (-i\Omega - \gamma_\perp)\mathcal{P} - i\frac{g^2}{\hbar}\mathcal{E}\mathcal{D} \tag{1b}$$

$$\dot{\mathcal{D}} = -\gamma_\parallel\left(\mathcal{D} - \mathcal{D}^0\right) + i\frac{2}{\hbar}\left(\mathcal{E}\mathcal{P}^* - \mathcal{E}^*\mathcal{P}\right) \tag{1c}$$

where $c = \frac{1}{\sqrt{\mu_0\epsilon_0}}$ is the speed of light in vacuum. We note that the above semi-classical MBEs describe the interaction of a cavity-confined electromagnetic field with a gain medium under some simplifying assumptions: (i) that the medium consists of homogeneous two-level atoms, and (ii) the interaction can be treated within the rotating-wave approximation [56, 57]. More general forms of MBEs relaxing some of these standard assumptions can also be considered [58–60]. A detailed derivation of the semi-classical MBEs from fully quantum-mechanical laser equations can be found in standard texts [61]. Mathematically, equations (1*a*)–(1*c*) most generally describe a set of coupled partial differential equations (PDEs) for arbitrary lasers. They must be accompanied by boundary conditions, here set by the geometry of the cavity confining the electric field. In this paper, we will consider the specific case of a ring laser (radius R and length $L = 2\pi R$), depicted schematically in figure 1(a), for which the boundary conditions must be periodic. This enables a simplification of the MBEs to a set of scalar PDEs, defined along the ring laser arc length coordinate, which we label x. Then, n_c is the effective refractive index of the cavity medium, which can be complex to incorporate cavity loss; in particular we write it as $n_c = n_R + in_I$. Phenomenological parameters $\gamma_\parallel$ and $\gamma_\perp$ represent the population and polarization decay rate, respectively, as shown in figure 1. Ω is the center frequency of the gain curve, g is the dipole moment, and $\mathcal{D}^0$ describes incoherent pumping threshold necessary to achieve population inversion and lasing. For simplicity, we consider a spatially homogeneous pump, although the spectral approach we employ can also account for nontrivial spatial pump profiles.

We begin by considering the standard approach to equations (1*a*)–(1*c*), namely employing the slowly-varying envelope approximation [62] to reduce the order of derivatives, reducing the wave equation for electric field evolution to an advection equation (or, in nonlinear optical media, the nonlinear Schrödinger's equation).

2.1. Slowly-varying envelope approximation

Within the standard slowly-varying envelope approximation, the form of the MBEs is simplified by explicitly extracting the spatiotemporal dependence at the frequency set by the atomic transition frequency. For ring lasers, this takes the form:

$$\mathcal{E}(x,t) = E_c \cdot \bar{E}(x,t)\frac{1}{\sqrt{L}}e^{i(n_R\Omega/c)x}e^{-i\Omega t} \tag{2a}$$

$$\mathcal{P}(x,t) = P_c \cdot \bar{P}(x,t)\frac{1}{\sqrt{L}}e^{i(n_R\Omega/c)x}e^{-i\Omega t} \tag{2b}$$

$$\mathcal{D}(x,t) = D_c \cdot \bar{D}(x,t) \tag{2c}$$

where we have also extracted dimensionful factors of the physical fields for convenience:

$$E_c = \frac{\hbar\sqrt{L\gamma_\perp\gamma_\parallel}}{2g}, P_c = \epsilon_0 E_c, D_c = \frac{\hbar\epsilon_0\gamma_\perp}{g^2}. \tag{3}$$

$\bar{E}(x,t)$, $\bar{P}(x,t)$ then describe the envelopes of the total electric and polarization fields respectively, which typically evolve at frequencies much slower than the large atomic transition frequency Ω that has been explicitly extracted. Substituting equations (2*a*)–(2*c*) into equations (1*a*)–(1*c*) and dropping terms proportional to the second-order time-derivative of the envelope fields defines the slowly-varying envelope approximation. The final MBEs under the slowly-varying envelope approximation take the form of an advection equation for the electric field (instead of a second-order wave equation), coupled to ODEs for the polarization and inversion fields:

$$\dot{\bar{E}} = -\frac{1}{n_R}\partial_x\bar{E} - \bar{\kappa}\bar{E} + i\frac{\bar{\Omega}}{2n_R^2}\bar{P} \tag{4a}$$

$$\dot{\bar{P}} = -\bar{\gamma}_\perp\bar{P} - i\bar{\gamma}_\perp\bar{E}\bar{D} \tag{4b}$$

$$\dot{\bar{D}} = -\bar{\gamma}_\parallel\left(\bar{D} - \bar{D}^0\right) + i\frac{\bar{\gamma}_\parallel}{2}\left(\bar{E}\bar{P}^* - \bar{E}^*\bar{P}\right) \tag{4c}$$

where we have also introduced the dimensionless space, time, and frequency scales:

$$\bar{x} = \frac{x}{L},\ \bar{t} = \frac{t}{L/c},\ \left(\bar{\Omega},\bar{\gamma}_\parallel,\bar{\gamma}_\perp,\bar{\kappa}\right) = \frac{L}{c}\left(\Omega,\gamma_\parallel,\gamma_\perp,\kappa\right) \tag{5}$$

and where $\bar{D}^0 = \frac{D^0}{D_c}$, while $\bar{\kappa} = \frac{n_I}{n_R}\bar{\Omega}$ describes the cavity loss rate proportional to the imaginary part of the refractive index.

Having introduced the various scaling transformations via equations (3) and (5), we will now drop the $\bar{(\cdot)}$ notation in the remainder of this paper, for clarity of the presentation. All quantities from here on are therefore to be understood as dimensionless, unless otherwise noted.

Equations (4*a*)–(4*c*) and their associated periodic boundary conditions still describe a set of PDEs, and thus must be solved using a spatio-temporal integration scheme such as a FDTD method. While well-established, such schemes are computationally expensive and scale unfavourably with system size. In the following sections, we develop an efficient spectral approach to capturing *dynamics* of complex multimode lasers described by the MBEs, and then benchmark this approach against more standard numerical techniques for simulating equations (4*a*)–(4*c*).

3. Multimode CFTD approach for laser dynamics

Any spectral approach to analyzing laser dynamics uses a spatial basis to project equations (1*a*)–(1*c*), thereby yielding a set of *ordinary* differential equations. The distinguishing feature of the CFTD spectral approach is the use of a general set of non-Hermitian modes as a basis: the constant-flux (CF) modes. In a multi-dimensional domain $\mathcal{R}$, the CF modes $\{\varphi_m(\boldsymbol{r},\Omega_c)\}$ are solutions to the generalized eigenproblem (in normalized units) $\nabla^2\varphi_m = -n_c^2(\boldsymbol{r})\omega_m^2\varphi_m$, with complex eigenfrequencies $\{\omega_m\}$. Crucially, the CF modes satisfy a specific outward-traveling solution past the boundary of the spatial domain $\partial\mathcal{R}$, imposed by outgoing boundary conditions $\frac{\partial\varphi_m}{\partial r}\big|_{\partial\mathcal{R}} \sim i\Omega_c\varphi_m$ [53, 63]. The CF modes are thus parameterized by an additional frequency Ω_c that determines this outgoing solution. Such boundary conditions correctly account for losses due to the fields leaking out of the laser cavity, thereby crucially rendering the eigenproblem defining the CF modes to be *non-Hermitian*. The CF basis has successfully provided the foundation for

Steady-state *Ab Initio* Lasing Theory (SALT) [52, 64], but only tackles a subset of temporal phenomena in lasers (to be made more precise in due course). The CFTD approach introduced in [53] for time *dynamics* aims to capture more complex temporal phenomena, as we will demonstrate.

For the ring laser systems considered in the original RNGH and LH models, some simplifying assumptions reduce the complexity of the aforementioned eigenproblem. A complex but uniform refractive index $n_c(\boldsymbol{r}) \to n_c$ was assumed as the only source of losses, and radial leakage was hence ignored. This additionally allows one to consider modes in an effectively one-dimensional geometry, by taking $\boldsymbol{r} \to x$, $\varphi_m(\boldsymbol{r}) \to \varphi_m(x)$ where x denotes the angular variable along the ring cavity. In the absence of radial leakage, the modes are then constrained simply by periodic boundary conditions.

Even with these simplifications, however, the eigenproblem of interest remains non-Hermitian: this is due to the presence of absorptive losses, rendering n_c complex-valued. The general formulation of CFTD [53] is built precisely for modes defined by non-Hermitian eigenproblems, regardless of whether the non-Hermiticity arises due to absorptive losses as here, or via radiative leakage more generally. Formally, the modes $\{\varphi_m(x)\}$ can be defined as eigenmodes of an operator $\mathcal{H}$,

$$\begin{aligned} \mathcal{H}\varphi_m(x) \equiv -\frac{1}{n_c^2}\nabla^2\varphi_m(x) &= \omega_m^2\varphi_m(x) \\ \varphi_m(x+1) &= \varphi_m(x). \end{aligned} \tag{6}$$

The operator $\mathcal{H}$ is non-Hermitian [65], since $n_c \neq n_c^*$ (see proof in appendix C). As a result, understanding its spectrum also requires evaluation of the dual eigenmodes $\{\widetilde{\varphi}_m(x)\}$ (referred to as 'left' eigenmodes in non-Hermitian matrix theory), defined via the associated adjoint operator:

$$\begin{aligned} \mathcal{H}^*\widetilde{\varphi}_m(x) \equiv -\frac{1}{n_c^{*2}}\nabla^2\widetilde{\varphi}_m(x) &= \omega_m^{*2}\widetilde{\varphi}_m(x) \\ \widetilde{\varphi}_m(x+1) &= \widetilde{\varphi}_m(x). \end{aligned} \tag{7}$$

It can be shown that for non-Hermitian operators, it is the left and right eigenmodes that satisfy the generalized orthogonality relation:

$$\int_0^1 dx\, \widetilde{\varphi}_m^*(x)\,\varphi_n(x) = \delta_{mn} \tag{8}$$

where the integral is defined over the spatial domain of the laser cavity. We will use these modes of the non-Hermitian operator $\mathcal{H}$ as our spatial basis.

The right eigenmodes obtained by solving the resulting equation (6) for a ring cavity by imposing periodic boundary conditions then take the simple form of propagating plane waves:

$$\varphi_m(x) = e^{ik_m x} \tag{9}$$

where $k_m = 2m\pi, m \in \mathbb{Z}$ is the wavevector for the mode indexed by integer m. The left eigenmodes can be similary obtained (see appendix C). The complex eigenfrequencies ω_m can be found exactly, and are parameterized in terms of their real parts ν_m describing the mode frequencies and imaginary parts κ_m describing losses:

$$\omega_m = \nu_m - i\kappa_m, \quad \nu_m = \frac{1}{n_\mathrm{R}}k_m, \quad \kappa_m = \frac{k_m}{n_\mathrm{R}}\frac{n_\mathrm{I}}{n_\mathrm{R}}. \tag{10}$$

The cold cavity mode spacing Δ [or free spectral range (FSR)] is constant and is given by $\Delta = \frac{2\pi}{n_\mathrm{R}}$. It is then clear that the orthogonality relationship of equation (8) is simply that of the complex Fourier basis.

Having defined our spatial basis modes, we will now return to the lasing cavity case and expand the coupled slowly-varying envelopes of the electric field and polarization using the following ansätze:

$$E(x,t) = \sum_m E_m(t)\,\varphi_m(x) \tag{11a}$$

$$P(x,t) = \sum_m P_m(t)\,\varphi_m(x). \tag{11b}$$

The spatial complexity of the laser cavity including boundary conditions is entirely captured by the cavity modes $\{\varphi_m(x)\}$, while the nontrivial time dynamics are encoded in the expansion coefficients

$\{E_m(t), P_m(t)\}$. We then substitute equations (11*a*) and (11*b*) into the MBEs (equations (1*a*)–(1*c*)), and make use of the orthogonality relationship to integrate out the spatial degrees of freedom over the ring cavity domain. Doing so also projects the inversion onto a set of the basis modes via:

$$D_{mn}(t) = \int_0^1 \mathrm{d}x\, \widetilde{\varphi}_m^*(x)\, D(x,t)\, \varphi_n(x)\,. \tag{12}$$

For the special case of a ring cavity, using the explicit form of the spatial basis modes, it is clear that $D_{mn}(t)$ are simply the spatial Fourier components at the wavevector *difference* $k_n - k_m$ of the inversion field at a time t. This special form of modal expansion for ring lasers has been employed earlier [30], albeit by explicitly assuming a Fourier expansion of the light and matter degrees of freedom at the outset. Instead, the projection and resulting dynamical equations we consider here are more general, being valid for basis modes that are not simply complex exponentials, and reduce to the Fourier expansion as a special case.

Leaving details of the spatial projection for appendix D, we present the final equations of motion for the variables $\{E_m, P_m, D_{mn}\}$ below:

$$\dot{E}_m = \frac{i}{2\Omega}\left(\Omega^2 - \nu_m^2 + \kappa_m^2\right) E_m - \kappa_m E_m + \frac{i\Omega}{2n_{\mathrm{R}}^2} P_m \tag{13a}$$

$$\dot{P}_m = -\gamma_\perp P_m - i\gamma_\perp \sum_n E_n D_{mn} \tag{13b}$$

$$\dot{D}_{mn} = -\gamma_\parallel \left(D_{mn} - D_{mn}^0\right) + \frac{i\gamma_\parallel}{2} \sum_{rs} \mathcal{A}_{mrsn}\left[E_r P_s^* - E_s^* P_r\right] \tag{13c}$$

where we have introduced the dimensionless mode overlap tensor $\mathcal{A}_{mrsn}$:

$$\begin{aligned}\mathcal{A}_{mrsn} &= \int_0^1 dx\, \widetilde{\varphi}_m^*(x)\, \varphi_r(x)\, \varphi_s^*(x)\, \varphi_n(x) \\ &= \int_0^1 \mathrm{d}x\, e^{i(k_n + k_r - k_m - k_s)x} = \delta(n + r - m - s)\,.\end{aligned} \tag{14}$$

The second line above specializes the tensor to the case of multimode ring lasers. Finally, we note that D_{mn}^0 defines the projected matrix elements for the incoherent pump, and is defined analogously to equation (12), with $D(x,t) \to D^0$. This definition can equivalently be used for spatially inhomogeneous pump profiles.

Equations (13*a*)–(13*c*) thus define the CFTD description of multimode dynamics for ring lasers: a time-domain description derived from the underlying spatiotemporal MBEs via a specialized spatial projection onto modes generally satisfying a non-Hermitian boundary value problem. The general notation we have used in our derivation emphasizes that the spatial modes can satisfy a broader class of non-Hermitian eigenproblems, for arbitrary geometries in multiple dimensions including random lasers [66], and incorporating losses via open boundary conditions [52].

3.1. Dynamics across regimes of stationary and non-stationary inversion

The assumption of stationary inversion, $\dot{\mathcal{D}}(t) = 0$, forms the basis of successful steady-state spectral descriptions of lasing, such as SALT. However, this assumption places strong constraints on lasing phenomena described by the MBEs. To see this, note that if the inversion is stationary equations (1*a*) and (1*b*) for the electric and polarization fields form a set with no nonlinear mixing of *time-dependent* terms. While the inversion does depend nonlinearly on $\mathcal{E}$ and $\mathcal{P}$ via equation (1*c*), it is assumed to be time-independent and hence does not lead to any frequency mixing in equations (1*a*) and (1*b*). The same observation holds for the subsequently-derived CFTD equations. Stationary inversion thus precludes the generation of new frequencies via intermodulation products of the lasing field and the gain medium population dynamics (which are strongly suppressed). New frequencies can arise in this regime, but via standard multimode lasing: with increasing pump power, a new spatial mode φ_m can lase if a corresponding pump threshold is crossed. These pump thresholds provide a natural truncation scheme within SALT, determining when a specific mode begins to lase and hence must be included in the spectral description.

In contrast, CFTD is not bound by the stationary inversion approximation, and is able to simulate dynamics across regions of both stationary *and* non-stationary inversion. For aforementioned regimes where SALT is valid, the CFTD ansatz can capture lasing modes φ_m with nonzero coefficients $E_m(t)$ containing only a single frequency in the long-time limit, defining the lasing frequency for that mode m. However, by allowing $E_m(t)$ to have more a general time dependence, CFTD can also capture *transient* dynamics where

the inversion evolves with time, to the final steady-state lasing regime where SALT operates; we discuss this dynamics in section 4. We note that correspondence between CFTD and SALT in regimes where the stationary inversion approximation is briefly violated were also investigated in [53].

Most importantly, in this paper we analyze regimes where the dynamics of the inversion give rise to lasing phenomena that are *qualitatively* different from multimode lasing: instabilities that lead to simultaneous generation of multiple coherent frequencies from a single lasing frequency background. The coefficients $E_m(t)$ associated with distinct spatial modes now have much more general, coupled dynamics: several coefficients can become nonzero simultaneously past a single threshold, instead of sequentially with multiple thresholds. Each $E_m(t)$ can even possess multiple distinct frequency components, a feature increasingly prevalent in more complex laser geometries [57]. This more general class of dynamics is the main focus of this paper, and the subject of sections 5 and 6.

3.2. Numerical verification

We investigate the accuracy and efficiency of the CFTD model by comparing against standard numerical approaches to simulating equations (4*a*)–(4*c*). The most natural comparison of the CFTD method, which is geometry-agnostic, is against a completely general spatiotemporal FDTD scheme. For specific comparisons, however, we also employ the split-step Runge-Kutta method (SSRK) [67, 68]. This scheme is tailored to ring lasers, and hence can be expected to perform optimally for the present case, but lacks generalizability to other geometries. We begin with comparisons in both simple single-mode lasing regimes but with nontrivial initial spatial field distributions (i.e. spanning multiple cavity modes) in section 4. When this single-mode lasing state becomes unstable, complex multimode lasing dynamics can ensue, including the formation of frequency combs which we analyze in section 5 or even the emergence of chaotic dynamics, discussed in section 6.

4. Single-mode lasing dynamics

We will begin our analysis of lasing dynamics with the simplest operating regime: single-mode lasing. Within our spectral approach, the single-mode lasing regime is characterized by restricting the expansion coefficients in equations (11*a*) and (11*b*) to the single-mode forms:

$$\begin{aligned} E_m(t) &= \delta_{lm} E_l(t) \\ P_m(t) &= \delta_{lm} P_l(t). \end{aligned} \tag{15}$$

so that the only mode with nonzero expansion coefficients is indexed by l, and is thus the solitary mode that lases. By virtue of how the inversion matrix elements are constructed—as projections onto the modes constituting the expansion of equations (11*a*) and (11*b*) - the resulting inversion matrix elements, equation (12), similarly reduce to:

$$D_{mn}(t) = \delta_{lm}\delta_{ln} D_{ll}(t). \tag{16}$$

As mentioned earlier, we consider a lasing cavity that experiences a spatially uniform pump gain and uniform loss profile. This is not a restriction of CFTD, but is a simplification we make for convenience of later comparisons. Under this assumption, it is easily found that the mode with lowest threshold pump power is one that is spectrally closest to the atomic transition frequency Ω (for details see appendix E),; we index this mode by $l = 0$, so by definition $|\nu_0 - \Omega| \ll |\nu_l - \Omega| \; \forall \; l \neq 0$. We emphasize, however, that this simple result holds provided the gain and loss distribution in the laser cavity is uniform. To simplify the analysis further, we consider a cavity such that $\nu_0 \simeq \Omega$, in which case the lasing occurs at the frequency Ω. This frequency is explicitly extracted in the CFTD ansätze, equations (11*a*) and (11*b*), so that the lasing mode in this frame is at zero frequency. As a result, the steady-state fields $E_0 = E_{ss}, P_0 = P_{ss}, D_{00} = D_{ss}$ in the single-mode lasing regime are all stationary, and are given by:

$$D_{ss} = D_{th} = \frac{2n_R^2\kappa}{\Omega}, \; |E_{ss}|^2 = \frac{D_{00}^0}{D_{th}} - 1, \; P_{ss} = -iE_{ss}D_{ss}. \tag{17}$$

Details of the derivation of the above expression can be found in appendix E.

In this single-mode regime, it would appear that a spectral approach retaining only the mode that eventually lases would suffice, namely restricting equations (11*a*)–(12) to $m = n = l = 0$. However, our more general ansätze allows us to quantitatively capture dynamics that require modes beyond the lasing mode, for

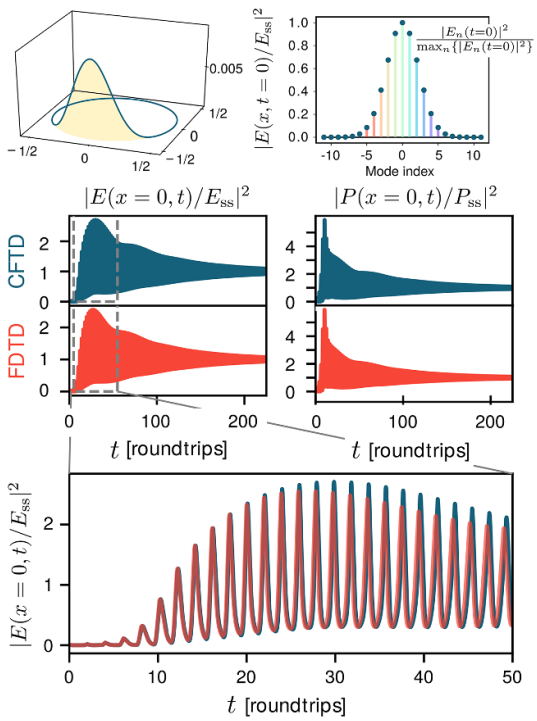

Figure 2. Multimode dynamics below the instability threshold (the pump power normalized by the single mode lasing threshold is $p = 5$). Top left panel shows the initial Gaussian electric field profile, $E(x, t = 0) = 0.1e^{-100x^2}$, scaled by E_{ss}. Projection of this initial profile on the CFTD spatial basis is shown in the top right plot. Center panel: comparison of dynamics of the electric field intensity $|E(x = 0, t)|^2$ and polarization $|P(x = 0, t)|^2$ using CFTD (blue) and FDTD (red). Lower panel shows $|E(x = 0, t)|^2$ scaled by E_{ss} for the first few roundtrips to highlight the agreement. Loss parameters are $\gamma_\perp = 5.0, \gamma_\parallel = 0.5, \kappa = 0.1$, while $n_R = 1.96$. The number of modes included is $N = 11$, the minimum for reproducing an accurate Gaussian profile as the initial condition.

example pulsed initial conditions or spatially non-uniform pumping schemes that excite modes other than the lasing mode, even if such modes decay away in the long-time limit.

To simulate this nontrivial regime, we explore the multimode dynamics of a ring laser pumped above the single-mode lasing threshold, with an initial intensity distribution within the laser cavity that is described by a Gaussian profile. We consider pumping the laser at a power five times above the single-mode lasing threshold, $p = \frac{D_{00}^0}{D_{th}} = 5$, with decay parameters $\gamma_\perp = 5.0, \gamma_\parallel = 0.5, \kappa = 0.1$, cold cavity refractive index set to $n_R = 1.96$, and then simulate the dynamics of the electric and polarization fields at a fixed position $x = 0$ of the ring cavity as a function of time, using both FDTD simulations of equations (4*a*)–(4*c*), and integration of the CFTD equations (13*a*)–(13*c*). The CFTD approach here takes into consideration modes $m \in -5, \ldots, 5$ for a total of $N = 11$ modes. A time-step $\Delta t = 2.45 \times 10^{-4}$ in units of roundtrips is used for FDTD simulations, while CFTD employs an ODE solver with an adaptive time-step.

The results are plotted in figure 2, in red for the FDTD simulations and blue for the CFTD simulations. We find excellent quantitative agreement between the two approaches; the lower panel zooms in on a length of time equal to 50 roundtrips, plotting both CFTD and FDTD results to highlight the agreement. Under stationary inversion, only a single-mode solution exists (see appendix E). However, the nontrivial time evolution indicates multimode dynamics in a transient period of ∼200 roundtrips after which a single mode lases in the long-time limit. The CFTD dynamics are substantially more efficient to simulate than the FDTD, requiring simulation times that are about two orders-of-magnitude shorter than the FDTD for the same timestep in regimes captured by several cavity modes (a more detailed comparison of CFTD simulation times versus the number of retained modes in more complex dynamical regimes is shown in section 7).

A unique aspect of the CFTD approach is the use of a projected set of inversion matrix elements $D_{mn}(t)$, equation (12), to capture the dynamics of the inversion field. Formally, this projection cannot be straightforwardly inverted to extract the spatio-temporal inversion field $D(x, t)$. For the case of a ring laser, these matrix elements have a simple physical interpretation. For a spatially-uniform inversion field, $D(x, t) = D(t)$, all off-diagonal inversion matrix elements vanish, as is seen from equation (12) and the orthogonality relationship, equation (8). This case represents the single-mode lasing regime for ring lasers.

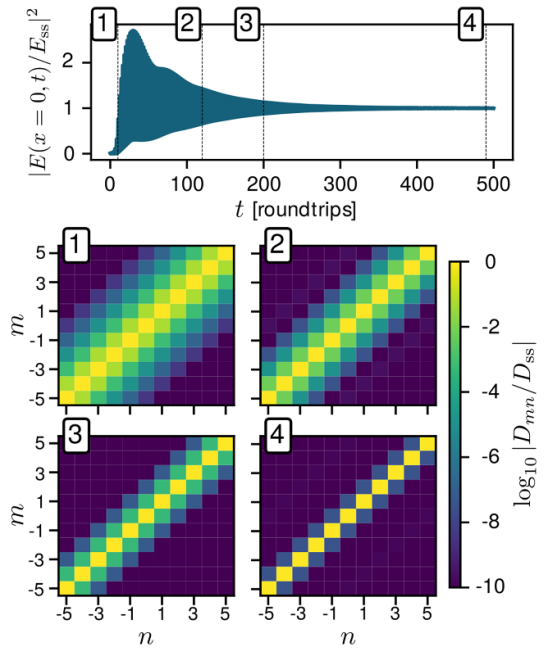

Figure 3. Top panel: Evolution of the electric field intensity in the single-mode lasing regime for 500 roundtrips. Bottom panel: Dynamics of inversion matrix elements $D_{mn}(t)$ in CFTD, evaluated at labeled time points, below the single-mode instability threshold ($p = 5$) for an initial Gaussian electric field profile corresponding to figure 2. Parameters are the same as that figure. Off-diagonal elements of the matrix are suppressed as the solution reaches the single-mode steady state.

However, when multiple spatial modes with distinct wavevectors are active, a spatial inversion grating is established in the laser cavity [34]: $D_{mn}(t)$ then precisely represent the time-evolution of spatial Fourier components of the inversion field at the *difference* of wavevectors $k_n - k_m$. For more general cavities where the projecting modes $\{\varphi_m(x)\}$ are not simply Fourier basis elements, $D_{mn}(t)$ for $n \neq m$ still represents the amplitude of this inversion grating.

The evolution of the inversion matrix elements can be seen in figure 3, where $D_{mn}(t)$ are plotted in the 2D plots at indicated time values 1 through 4 scaled by the single-mode lasing steady-state inversion, D_{ss}. For the first ≈200 roundtrips the multimode initial pulse is travelling through and in fact building up in the ring laser, and this dynamics leads to the generation of off-diagonal inversion matrix elements due to the inversion grating. However, with increasing time, additional modes decay away and the laser returns to a single-mode lasing state; concurrently, the off-diagonal inversion matrix elements are suppressed.

We thus see that the CFTD can accurately capture spatiotemporally-complex initial conditions in the regime of single-mode lasing. With increasing pump power, it is natural to ask whether the single-mode lasing regime analyzed in this section breaks down, and if other cavity modes can be coherently excited in the long-time limit, unlike the dynamics observed in figure 2. This is the subject of the next section.

5. Coherent multimode lasing dynamics: RNGH instability

It can be shown that uniformly incoherently-pumped ring lasers experience gain clamping above the single-mode lasing threshold. The inversion field attains a stationary, spatially-homogeneous value, and prevents additional modes from crossing the lasing threshold while the first mode is still lasing. However, this does not mean that multi-mode dynamics cannot ensue: other types of instabilities do exist, where the single lasing mode itself becomes unstable, leading to the generation of new frequencies mediated by the gain medium. Such a regime is marked by the inversion field becoming time-dependent, leading to so-called *population pulsations* [27].

The LH and RNGH instabilities [32, 33] represent prototypical examples of such a strongly-pumped, nonlinear multimode lasing regime. The salient features of these instabilities were originally predicted via a spatiotemporal linear stability analysis (ST LSA) of the MBEs [32] and then verified numerically; these features are summarized in figure 4 and discussed below. Above a critical (normalized) pump power that we refer to as the *instability threshold* p_{th} (the so-called second threshold in early literature),

$$p_{\text{th}} = 5 + 3\left(\frac{\gamma_{\parallel}}{\gamma_{\perp}}\right) + 2\sqrt{4 + 6\left(\frac{\gamma_{\parallel}}{\gamma_{\perp}}\right) + 2\left(\frac{\gamma_{\parallel}}{\gamma_{\perp}}\right)^2}, \tag{18}$$

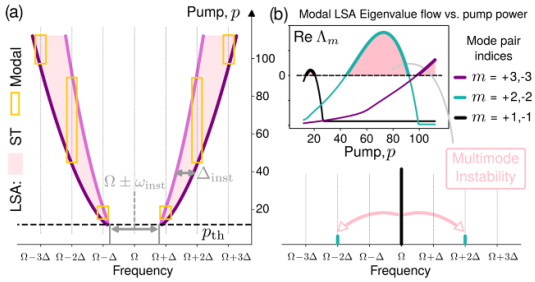

Figure 4. (a) ST LSA results based on the original formulation of Risken and Nummedal [32], and corresponding modal LSA results. Beyond a specific pump threshold p_{th} [see equation (18)], the single-mode lasing solution becomes unstable, at a frequency given by ω_{inst}. Dashed lines indicate the results of the modal LSA based on linearization of the CFTD equations. (b) Real part of the eigenvalues Λ_m of the dynamical matrix in equation (21) as a function of pump power. A positive real part indicates an instability. Specific ring laser parameters considered here are $\gamma_\perp = 1.0, \gamma_\parallel = 0.5, \kappa = 0.1$, and $n_{\text{R}} = 1.96$.

the single-mode lasing solution becomes unstable (see red dashed red line in figure 4), giving rise to symmetric sidebands at the frequencies $\Omega \pm \omega_{\text{inst}}$. At higher pump powers, a continuous range of frequencies as marked by the shaded region are predicted to be unstable; the width of this region in frequency is given by Δ_{inst}.

Here, we note the distinction that is often made in the literature, according to the ratio of the gain linewidth $\gamma_\perp$ to the FSR Δ. In particular, for $\gamma_\perp/\Delta < 1$, a single cavity mode—the lasing mode—falls under the gain curve. The resulting instability is referred to as the single-mode or LH instability. In the opposite regime where $\gamma_\perp/\Delta > 1$, several cavity modes fall under the gain curve; consequently, the emerging instability is labeled the multi-mode or RNGH instability. While dynamics in both regimes can be distinct (as we will see), both are described by the same ST LSA, with different parameters.

In specific parameter regimes, these ST LSA results can be cast in simplified analytic forms. In particular, in the RNGH case and further considering $\gamma_\perp \gg \Delta, \gamma_\parallel, \kappa$, the minimum unstable frequency and the range of unstable frequencies close to the instability threshold p_{th} take the forms [32],

$$\pm\omega_{\text{inst}} = \pm\gamma_\perp \left(2\sqrt{3} - \frac{2}{\sqrt{3}}\frac{\kappa}{\gamma_\perp}\right)\sqrt{\frac{\gamma_\parallel}{\gamma_\perp}} \tag{19a}$$

$$\Delta_{\text{inst}} \simeq \gamma_\perp \left(\frac{\sqrt{6}}{2} + \frac{7}{\sqrt{6}}\frac{\kappa}{\gamma_\perp}\right)\sqrt{\frac{\gamma_\parallel}{\gamma_\perp}}\sqrt{\frac{p}{p_{\text{th}}} - 1}. \tag{19b}$$

Note that both ω_{inst} and Δ_{inst} generally grow with $\gamma_\perp$. While the magnitude of this linewidth in comparison to the FSR ($\gamma_\perp/\Delta$) is heuristically understood to increase the participation of cavity modes in lasing, here we see its role in increasing the participation of modes in multimode instabilities. As we will see via numerical simulations, this increase in Δ_{inst} via $\gamma_\perp/\gamma_\parallel$ will lead to a growing complexity of multimode dynamics.

Having described the general multimode instability, we now discuss how the CFTD approach can also predict this instability using an efficient modal linear stability analysis (*modal* LSA).

5.1. Modal LSA: instability via non-stationary inversion

Within the CFTD approach, instability of the single-mode lasing solution arises naturally via the growth of unstable sidebands for $m \neq 0$. We analyze the dynamics of these sidebands in a linearized approximation:

$$E_m = E_{\text{ss}}\delta_{0m} + \delta E_m + O\left(\delta E_m^2\right) \tag{20a}$$

$$P_m = P_{\text{ss}}\delta_{0m} + \delta P_m + O\left(\delta P_m^2\right) \tag{20b}$$

$$D_{mn} = D_{\text{ss}}\delta_{mn} + \delta D_{mn} + O\left(\delta D_{mn}^2\right) \tag{20c}$$

and retaining only terms to linear order in $\{\delta E_m, \delta P_m, \delta D_{mn}\}$.

The multimode LSA then proceeds by first obtaining linearized dynamical equations for the sideband fluctuations and inversion matrix elements. Leaving details of the derivation for appendix F, the resulting equations can be conveniently written in matrix form as:

$$\frac{d}{\mathrm{d}t}\begin{pmatrix}\delta\vec{v}_m \\ \delta\vec{v}_{-m}\end{pmatrix} \equiv \mathcal{M}_m\begin{pmatrix}\delta\vec{v}_m \\ \delta\vec{v}_{-m}\end{pmatrix} = \begin{pmatrix}\mathbf{J}_m & \mathbf{C}_{m,-m} \\ \mathbf{C}_{m,-m} & \mathbf{J}_{-m}\end{pmatrix}\begin{pmatrix}\delta\vec{v}_m \\ \delta\vec{v}_{-m}\end{pmatrix} \tag{21}$$

where the component vectors $\delta\vec{v}_m$ include fluctuation variables for mode m:

$$\vec{v}_m = (\delta E_m, \delta E_m^*, \delta P_m, \delta P_m^*, \delta D_{0m}, \delta D_{0m}^*)^T. \tag{22}$$

Immediately, we note that a closed set of linearized equations can only be obtained when considering the coupled dynamics of *pairs* of modes $\{m, -m\}$. Here $\mathbf{J}_m$ is a 6-by-6 dynamical matrix of the fluctuations of mode m alone, including those of the inversion matrix elements. Importantly, the dynamics due to $\mathbf{J}_m$ alone lead to a decay of the mth mode fluctuations in the long-time limit, so that the single-mode lasing solution ($m = 0$) remains stable.

However, the matrix $\mathbf{C}_{m,-m}$ couples fluctuations of different modes, in particular the symmetric mode pair $\{m, -m\}$. As $\mathbf{J}_m$ does not lead to instability, any multimode instabilities arise due to this coupling matrix. Crucially, as we show in appendix F, the coupling is mediated by nonzero *off-diagonal* inversion matrix elements D_{0m}, namely $\pm m \neq 0$. For a ring laser with *stationary* inversion, the inversion is also spatially homogeneous, and from equation (12) will thus only lead to nonzero *diagonal* inversion matrix elements D_{mm}. As a result, the requirement of $D_{0m} \neq 0$ for nonzero m in a ring laser necessitates non-stationary inversion, accounted for within the framework of CFTD.

We now present results of the CFTD stability analysis enabled by equation (21), which evaluates the stability of each mode pair $\{m, -m\}$ via the eigenvalues of the dynamical matrix $\mathcal{M}_m$. As an example, we plot the largest real part of the eigenvalue spectrum, Re Λ_m, for a selection of mode pairs in figure 4, as a function of pump power. We see that with increasing pump power, the eigenvalue for a specific mode pair can cross the instability threshold (its real part becomes positive). These shaded regions correspond to mode pairs experiencing gain and growing around the single-mode lasing solution, as depicted in the lower panel. However, note that the eigenvalue flow can be highly monotonic, so that a specific mode pair can become sub-threshold again with increasing pump power. At any pump power, the predicted unstable mode pairs are marked with solid lines in figure 4(a), where they coincide perfectly with the RNGH instability region for the parameters considered.

Importantly, pump powers also exist where the CFTD modal LSA predicts no unstable mode pairs. For such pump powers, the RNGH stability analysis predicts an unstable frequency, but this frequency does not coincide with that of a cold cavity mode (dotted vertical lines). The CFTD analysis indicates that for such pump powers, there will be no multimode instability; we will verify these predictions numerically in the following section.

We note that the modal LSA derived here takes a similar form to earlier work on ring lasers [30] where modal expansions of MBEs have been considered, and also agrees with the original ST LSA for the considered parameters. However, this modal LSA is based on a more general expansion that could be applied to studying multimode instabilities in alternative laser geometries.

5.2. Good cavity regime and slow polarization relaxation $\gamma_\perp/\gamma_\parallel \lesssim 2.0$

We are now in a position to simulate the dynamics of ring lasers in parameter and pump regimes where both the approximate ST stability analysis and its modal counterpart enabled by CFTD predict multimode instabilities. We will do so by integrating the exact CFTD equations, equation (13), and compare the results against integration of the MBEs under the slowly-varying envelope approximation, equations (4*a*)–(4*c*). To begin, we focus on the 'good cavity' regime where $\kappa < \gamma_\perp + \gamma_\parallel$, considering $\gamma_\perp = 1.0, \gamma_\parallel = 0.5, \kappa = 0.1$ and $n_R = 1.96$; dynamics in the 'bad cavity' limit are analyzed in section 6. Note that $\gamma_\perp < \Delta = \frac{2\pi}{n_R}$, so the emergent instability would typically be characterized as of the LH type. Finally, as the carrier and polarization decay rates are similar (hence, their ratio is relatively small ($\lesssim$10), this regime may be representative of so-called class A lasers, depending on the choice of κ. This class of lasers includes dye lasers, HeNe lasers and quantum cascade lasers.

We simulate the CFTD equations to obtain $\{E_m(t), P_m(t), D_{nm}(t)\}$ for $m \in -5, \ldots, 5$ (i.e. $N = 11$ spatial modes). This allows us to reconstruct the electric field using equation (11*a*), namely $E(x,t) = \sum_m E_m(t)\varphi_m(x)$, as a function of normalized pump powers p over a large range past the single mode lasing threshold, evolving for $t = 1000$ roundtrips at each pump power. This detailed study is greatly aided by the numerical efficiency of the CFTD equations, which provide a significant simulation speedup in comparison to spatiotemporal schemes like FDTD (see section 7). We first extract the resulting normalized frequency spectrum of the electric field at $x = 0$, $\mathcal{F}\{E(x=0,t)/E_{ss}|^2\}$, which is shown in figure 5(a), with amplitudes depicted according to the listed color scale.

Until the RNGH threshold p_{th} is reached, a single-mode lasing regime is clearly observed. Past this threshold, the predicted instability of single mode lasing dynamics is observed, giving way to a stable waveform exhibiting a frequency comb in its electric field frequency spectrum. Importantly, the dominant unstable sidebands occur at $\Omega \pm \Delta$, consistent with the prediction of both LSA methods. This instability

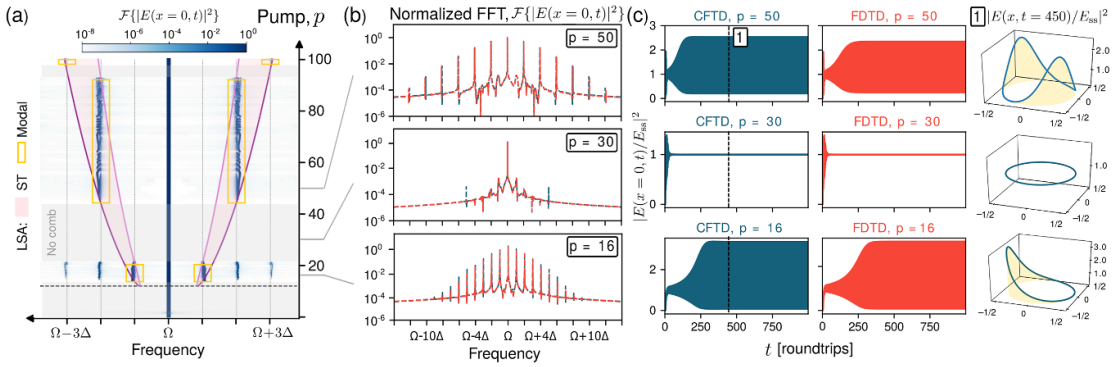

Figure 5. Emergence of frequency combs via the LH instability in ring lasers for loss parameters $\gamma_\perp = 1.0, \gamma_\parallel = 0.5, \kappa = 0.1$, and $n_R = 1.96$. (a) Frequency spectrum of the electric field as a function of pump power obtained using CFTD. Shaded regions mark the continuous frequencies predicted to be unstable by the ST LSA, while yellow boxes mark the discrete mode pairs predicted to be unstable by the modal LSA. Cold cavity mode frequencies are shown in dashed black, while the horizontal dashed line is the instability pump threshold p_{th}. (b) Normalized electric field spectra at specific pump powers, and (c) their corresponding time traces $|E(x=0,t)|^2$ scaled by E_{ss}, computed using both CFTD (blue) and FDTD (red) for a direct comparison. Right panel: Spatial distribution of the steady-state pulsing electric field in the ring cavity at a fixed time, $|E(x,t=450)/E_{ss}|^2$ (marked by (1) in (c)), computed using CFTD across the three pump powers simulated in the previous panels.

propagates to a broad frequency comb with a spacing of one FSR. A more detailed look at the observed comb is presented in figure 5(b) for $p = 16$, which also shows the comparison between CFTD and FDTD, finding excellent agreement. Figure 5(c) shows the CFTD and FDTD simulations in the time domain, demonstrating the ability of CFTD to capture not only the steady-state frequency comb but also the transient approach to this state.

Finally, the right panel of figure 5(c) shows the spatial electric field profile at $t = 450$ (roundtrips), reconstructed from the CFTD solution. In this particular regime, each $E_m(t)$ associated with the spatial mode φ_m evolves at a single dominant frequency; hence the multiple frequency components observed in figure 5(b) indicate a waveform that consists of several spatial modes of the cavity being coherently excited. This yields a localized propagating pulse in the laser cavity, sometimes referred to as a Turing roll in the spatiotemporal pattern formation literature [69]. We verify these CFTD results against the FDTD and SSRK (not shown), finding excellent agreement once more.

With increasing pump power, the frequency comb suddenly collapses back to stable single mode lasing operation. Here, even though the ST LSA predicts a continuous instability band, no specific mode falls into this band. The modal linear stability approach, on the other hand, predicts discrete pairs of unstable modes, and here finds no such pairs to be unstable, consistent with the simulated dynamics. At a representative pump power $p = 30$, the observed frequency spectrum in figure 5(b) using both CFTD and FDTD shows no comb formation, and the time traces in figure 5(c) exhibit no oscillations, instead settling into the single mode steady state solution E_{ss}, with a uniform spatial distribution as viewed in the right panel.

With further increase in pump power, the frequency comb emerges again, now with a 2-FSR spacing. Here, the unstable sidebands at $\Omega \pm 2\Delta$ fall in the instability region, and are also predicted to be unstable by the modal LSA. Again at the representative value of $p = 50$, CFTD and FDTD show excellent agreement in capturing the extent of the frequency spectrum of the comb in figure 5(b), oscillations in the time domain in figure 5(c), and the spatial profile in the rightmost panel, which now displays two peaks and half the propagation period, consistent with the higher spacing of peaks in the frequency spectrum.

In summary, in this regime of slower polarization relaxation, we find excellent quantitative agreement between FDTD simulations of the MBE and our CFTD approach, as well as between the ST LSA and its modal counterpart derived from the CFTD equations. We also note that in this regime, both methods agree with the SSRK method specific to ring lasers (not shown).

Importantly, some of the dynamics we have observed via simulations in this section have also been shown experimentally in this class of lasers, albeit at much lower pumping powers. In quantum cascade lasers in particular, the RNGH instability has been hypothesized to have a significantly lower onset threshold [3, 70]; other instability mechanisms have been explored as well [40]. Frequency combs containing on the order of ten modes arising from ring lasers have been demonstrated only recently [40, 41, 71]. So-called harmonic combs where modes skip several FSR lines, temporally leading to a waveform that repeats multiple times per round-trip, such as the one shown in figure 5(b) have also been experimentally demonstrated in modified ring cavities [72]. Temporal patterns such as Turing rolls have been theoretically predicted in quantum cascade lasers under a different instability mechanism [40] and solitons have only recently been

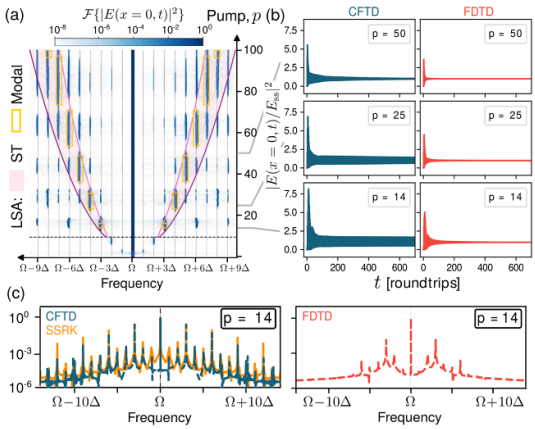

Figure 6. RNGH instability and comb formation for decay parameters: $\gamma_\perp = 10.0, \gamma_\parallel = 0.5, \kappa = 0.1$, and $n_R = 1.96$. (a) Frequency spectrum of electric field as a function of pump power obtained using CFTD. Shaded regions mark the continuous frequencies predicted to be unstable by the ST LSA, while yellow boxes mark the discrete mode pairs predicted to be unstable by the modal LSA. The horizontal dashed line marks the RNGH instability threshold. (b) Side by side comparison of $|E(x=0,t)|^2$ scaled by E_{ss} for the first 700 roundtrips of the CFTD (blue) and FDTD (red) results. The number of modes included in the CFTD simulations is $N = 19$. (c) Frequency spectrum of the electric field for $p = 14$ for CFTD (blue) and SSRK (orange) in the left panel, and FDTD (red) in the right panel, calculated for 1100 roundtrips. Note the qualitatively good agreement between the CFTD and the SSRK, and the significant deviations of FDTD.

experimentally verified [20, 73]. These experimental results illustrate the existence of multimode instabilities that could be well captured by the CFTD method applied to real laser devices.

In this vein, the parameters used in our analysis can be converted to dimensionful values using equation (5) for comparison with real devices. The parameters considered in this section correspond to $\gamma_\perp \approx$ 100 GHz, $\gamma_\parallel \approx 50$ GHz and $\kappa \approx 10$ GHz for a 3 mm cavity, or equivalently a ring laser with a radius of 477 μm. This cavity size is, for example, typical of monolithic mid-infrared lasers due to the relatively long wavelength of operation. While comparable, these decay rates are generally somewhat smaller than those of typical quantum cascade lasers [3, 20, 70], in particular the polarization decay rate; however, the physically-relevant parameter *ratios* are similar to those in standard quantum cascade lasers. This further encourages the application of the CFTD approach to analyze dynamics of contemporary laser devices.

5.3. Good cavity regime and slow polarization relaxation $\gamma_\perp/\gamma_\parallel \gtrsim 20.0$

The ratio $\gamma_\perp/\gamma_\parallel$ plays an important role in the features of the ST LSA as explained by equation (19*b*). Thus far we have explored regimes for which $\gamma_\perp/\gamma_\parallel \leq 2$, and have found the CFTD to provide excellent quantitative agreement with exact integration using FDTD, while providing the speedup advantages afforded by a temporal scheme as opposed to a spatiotemporal one. As the ratio $\gamma_\perp/\gamma_\parallel$ increases, both the threshold frequency at which instability occurs and the width of the instability band increase, leading to more involved comb formation dynamics at high pump powers. In these more complex regimes, we find that the CFTD still provides very good qualitative agreement with more numerically-expensive methods. For a concrete demonstration, we consider the ratio $\gamma_\perp/\gamma_\parallel = 20$, with decay parameters $\gamma_\perp = 10.0, \gamma_\parallel = 0.5, \kappa = 0.1$ (for supplementary simulations with different parameters, see appendix G). Now, $\gamma_\perp > \Delta$, so the emergent instability would generally be characterized as the RNGH instability. We note also that this case where the polarization decay rate is significantly larger than the population decay rate typically describes lasers in class B, depending on the value of κ [55]. This class includes lasers such as semiconductor lasers and solid state lasers.

As the ratio of decay parameters increases, so does the number of relevant modes that must be included in the simulation. In this case, the number of modes increases up to ~21 (corresponding to $\Omega \pm 10\Delta$). We then once again calculate the frequency spectrum of the electric field using CFTD, with the results shown in the left panel of figure 6.

With increasing pump power beyond the RNGH threshold p_{th}, a stable frequency comb emerges from the single-mode lasing state, as before. However the observed spacing is now equal to 3 FSRs, as the increased ratio of $\gamma_\perp/\gamma_\parallel$ increases the unstable mode frequency ω_{inst} via equation (B1). Importantly, the unstable mode pair is exactly that predicted by both LSA schemes. With further increase in pump power, the predicted unstable mode pair moves outwards relative to the single-mode lasing frequency. Importantly, the CFTD simulations show an increase in the comb FSR with pump power, consistent with both LSA methods.

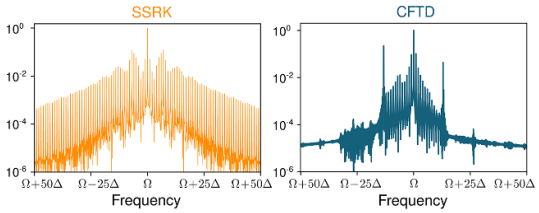

Figure 7. SSRK and CFTD comparison for decay parameters: $\gamma_\perp = 25.0, \gamma_\parallel = 0.5, \kappa = 0.1$, and $n_R = 1.96$. The selected pump power is $p = 30$. Shown on the left is the frequency spectrum of the electric field as computed Fourier Transform from 1100 roundtrips of the SSRK result showing more than 100 modes. Shown on the right is the frequency spectrum of the electric field as obtained from 1000 roundtrips of the CFTD with $N = 35$ modes included in the simulation.

Furthermore, the observed combs can even possess multiple, non-commensurate dominant frequency components, unlike the simpler dynamics at lower values of $\gamma_\perp/\gamma_\parallel$.

In contrast, in these regimes our benchmark FDTD method performs rather poorly. In figure 6(b), we compare simulated time traces using CFTD and FDTD for 700 roundtrips for three selected pump powers $p = 14$, $p = 25$ and $p = 50$. While CFTD demostrates sustained oscillations as necessitated by the comb spectra observed figure 6(a), the FDTD simulation exhibits a suppressed amplitude and quickly settles to E_{ss}. The difference is further highlighted by a detailed look at the frequency spectrum of the electric field at $p = 14$ shown in figure 6(c) for both CFTD and FDTD. The FDTD simulation clearly does not yield a broad frequency comb like the CFTD approach; rather the central mode and only two sidebands are the main active frequencies. The 'washing out' of higher frequency components is a known issue of FDTD methods, due to the increased rate of accumulation of phase errors of higher frequency components, whose the phase evolves more rapidly. By explicitly operating in the frequency domain, the CFTD appears more robust to such effects.

Deeper in this regime of fast polarization relaxation where increasing disagreements are observed between the CFTD and FDTD, the SSRK scheme provides a more exact method that can be used to understand the discrepancies. However, we recall at the outset that the SSRK is subject to a number of limitations. First, it is tailored to ring geometries only, whereas the CFTD can accommodate arbitrary geometries. Second, simulation times for the SSRK are similar to the FDTD; hence the CFTD remains a considerably faster method. Finally, the SSRK cannot be easily extended to simulate photonic molecule or other coupled laser arrangements.

With these caveats, we present comparisons of the CFTD against the SSRK in regimes of fast polarization relaxation, where the FDTD performs poorly. For $\gamma_\perp/\gamma_\parallel = 20$, the SSRK generally shows good agreement with the CFTD. An example of the electric field frequency spectrum in the unstable regime is shown in orange in the lower panel of figure 6 revealing a 3-FSR comb for $p = 14$; the prominent frequency peaks show good agreement with the corresponding spectrum using CFTD shown in blue in the left panel, and strongly disagrees with the FDTD in red in the right panel.

For even larger $\gamma_\perp/\gamma_\parallel$ ratios, we expect the CFTD to require the retention of even more spatial modes for simulation, leading to diminishing returns in terms of the relative simulation time advantage in comparison to the SSRK, and also possibly introducing numerical errors. We illustrate one such regime where $\gamma_\perp/\gamma_\parallel = 50$ in figure 7, showing the electric field frequency spectrum obtained using the SSRK method in orange and the CFTD in blue. We note that the SSRK predicts more than 100 distinct frequency components to be excited. In the CFTD simulation we include 35 spatial modes, which leads to a reasonable simulation time (shorter than for the SSRK) and no obvious numerical artefacts. While CFTD is not restricted to only exhibiting as many frequency components as included spatial modes (see [53, 57] and discussion in section 3.1), here we see the CFTD spectrum is significantly restricted in comparison to the SSRK. However, while CFTD may not be ideally suited to simulating such extremely broadband dynamics in ring lasers where the SSRK exists as an alternative, the generalizability to arbitrary geometries still makes CFTD an attractive proposition for analyzing multimode instabilities in more general laser systems.

6. Chaotic dynamics

Not all multimode instabilities yield desired stable frequency combs. In this section, we will show that the CFTD can also efficiently capture a broader class of multimode instabilities, namely chaotic lasing dynamics. To this end, we now consider a different parameter regime to our prior simulations: we maintain $\gamma_\parallel = 0.5$, but set $\gamma_\parallel/\gamma_\perp = 1$, and importantly now choose $\kappa = 1.1$, which is just large enough for the laser system to operate in the 'bad cavity' regime, where $\kappa > \gamma_\perp + \gamma_\parallel$. Note that we again have $\gamma_\perp < \Delta$, the regime of the LH instability, which in conjunction with the bad cavity limit is known to feature chaotic emission at high

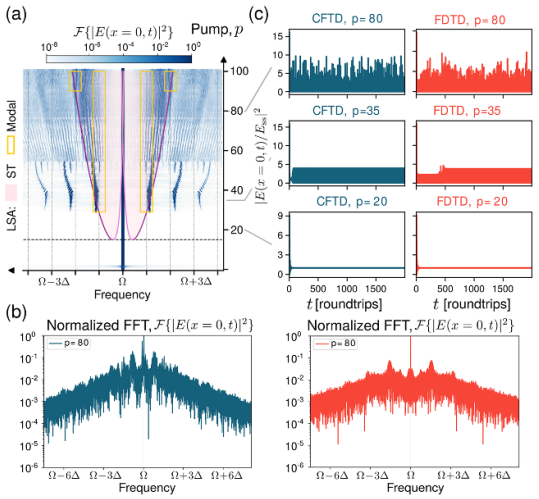

Figure 8. Emergence of chaotic behavior for decay parameters $\gamma_\perp = 0.5, \gamma_\parallel = 0.5, \kappa = 1.1$, and $n_R = 1.96$. (a) Frequency spectrum of the electric field as a function of pump power obtained using CFTD with $N = 17$ retained modes. Shaded regions mark the continuous frequencies predicted to be unstable by the ST LSA, while yellow boxes mark the discrete mode pairs predicted to be unstable by the modal LSA. The horizontal dashed line indicates the instability threshold. (b) Side by side comparison of $|E(x=0,t)|^2$ scaled by E_{ss} for the first 2000 roundtrips of the CFTD (blue) and FDTD (red) results. (c) Fourier Transform of $|E(x=0,t)|^2$ for $p = 80$ where we find chaotic behaviour in both the CFTD (blue) and FDTD (red) simulation.

pump powers [51, 74]. We now demonstrate that this is indeed the case, and analyze CFTD performance in such regimes.

In figure 8 we show the spectrum of the electric field as a function of pump power using CFTD. For pump powers past p_{th} up to around $p \sim 30$, the single-mode lasing regime persists. This is consistent with the modal LSA, which predicts no unstable mode pairs in this pump range, and the ST LSA as no cold mode frequencies fall in the predicted instability region. For higher powers up to $p \sim 55$, a stable frequency comb solution emerges, initially with an FSR predicted by both LSAs, but exhibiting complex frequency pulling at higher pump powers.

Such dynamics is similar to that observed in simulations in the good cavity regime in section 5. However, beyond $p \sim 55$, the spectrum of the electric field suddenly broadens into several finely spaced, but still coherent, peaks. At even higher pump powers around $p \sim 70$, however, any sharp peaks decohere into an elevated and extremely broad noise floor, features typical of chaotic regimes. This qualitative change in lasing dynamics coincides with regions where the instability bands of the ST LSA, which are symmetric with respect to the central frequency, start to overlap. Such an overlap requires a system operating in the bad cavity regime (see appendix B), as we consider here.

At a specific pump power $p = 80$ in this regime, a more detailed look at the frequency spectrum of the electric field is shown in figure 8(c), using both CFTD and FDTD schemes. Both show clear signatures of chaos: a broadband, noisy spectrum with several active frequencies and no significant coherent peaks. Time traces of the electric field using both CFTD and FDTD are also shown in figure 8(b). For $p = 80$, both methods are in good agreement, showing noisy traces with no recurrent oscillations. We also see that for specific pump powers in the other two aforemention regimes, CFTD and FDTD also show very good agreement.

We therefore clearly see that the CFTD is able to capture chaotic dynamics, as well as transitions from stable comb formation regimes to chaotic regimes. This makes the CFTD approach promising to identify—and avoid—regions of parameter space that do exhibit multimode instabilities, but do not allow useful, stable frequency comb formation.

7. Simulation time comparison

Having explored the numerical fidelity of the CFTD in comparison to more standard simulation schemes, we now quantify the speedup in simulation time provided by the CFTD. In figure 9, we show the simulation time for the CFTD as a function of the number of included modes N, and the simulation time for an equivalent FDTD integration for comparison. The results shown are for the laser system defined by parameters $\gamma_\perp = 5.0, \gamma_\parallel = 0.5, \kappa = 0.1$, $n_R = 1.96$, and a fixed pump power $p = 25$; however they are representative of the speedup typically observed using the CFTD. We note that to ensure a fair comparison, the number of roundtrips simulated and the spatial discretization used is kept the same between both methods.

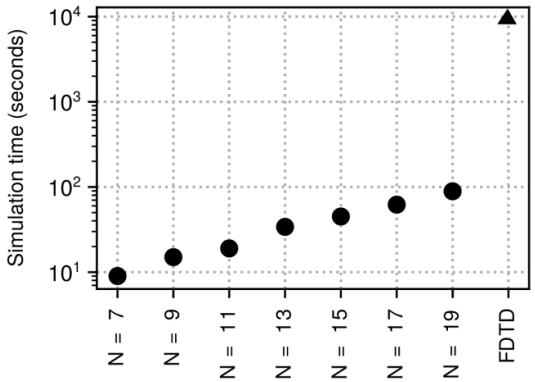

Figure 9. Simulation time comparison between the CFTD method for various numbers of modes included in the simulation (circles) and the FDTD method (triangle). The CFTD is at least two orders of magnitude faster, even when a relatively large number of modes is included in the simulation.

We consider various mode numbers from $N = 7$ to $N = 19$ for the CFTD, even though $N = 15$ is sufficient for the CFTD to yield accurate results in this particular example. The simulation time for the CFTD increases with the number of modes, but even for the highest mode numbers it remains about two orders of magnitude faster than the FDTD. This highlights one of the main advantages of our spectral CFTD approach: its computational speed, attained by the ability to reduce the integration of multidimensional PDEs to a set of ODEs in time only. The stark difference in the one-dimensional ring laser case explored here will only become larger for simulations of larger laser systems in two- or three-dimensions.

8. Conclusions and outlook

In this paper, we have demonstrated a spectral approach, CFTD, as a viable and efficient method to simulate one of the most complex time-dependent phenomena in lasers: the emergence and resultant dynamics of coherent multimode instabilities. Our approach projects the standard MBEs of laser dynamics onto a suitably chosen spatial basis accounting for the lasing cavity geometry and losses, obtaining a set of time-dependent coefficients of the electric field, polarization, as well as inversion which is captured via a projected set of matrix elements. Expanding far beyond our previous work [53], we have considered regimes where non-stationary inversion plays a crucial role in the emergence of coherent multimode instabilities. By benchmarking the CFTD method with an FDTD approach, as well as an SSRK scheme specific to ring lasers, we have found excellent qualitative agreement across a very wide parameter space, and quantitative agreement in regimes with up to $\approx$30 relevant modes. We reveal the ability to capture various waveforms and complex phenomena in our analysis, starting from single mode behavior to frequency combs of different FSR spacings to broadband chaotic spectra.

Our method provides not only an increase in simulation speed of at least two orders of magnitude over standard spatiotemporal integration schemes, but also more analytic insight into the system under study, via a linear stability analysis based on discrete included modes. While we have analyzed here a single ring laser, the CFTD method we introduce is a fast and efficient tool that can easily be extended to study complex time-dependent phenomena in much more general laser systems, a research area of significant contemporary interest. Such systems include complex cavity geometries without specific spatial symmetries, as well as coupled laser arrays. The complexity of analyzing such systems with conventional numerical schemes is substantial even in standard multimode lasing regimes (i.e. with stationary inversion), let alone coherent instabilities with nontrivial population dynamics. This only highlights the utility of the CFTD method.

Data availability statement

All data that support the findings of this study are included within the article (and any supplementary files).

Acknowledgments

This work was supported by the Eric and Wendy Schmidt Transformative Technology Fund and the National Science Foundation under Grant No. DMR-1610540. Simulations in this paper were performed using the Princeton Research Computing resources at Princeton University, which is a consortium of groups led by the

Princeton Institute for Computational Science and Engineering (PICSciE) and Office of Information Technology's Research Computing.

Appendix A. MBEs in the slowly-varying envelope approximation

A standard approach to analyzing the dynamics of the MBEs of equations (1*a*)–(1*c*) begins by extracting the fast frequency dependence from the atomic transition frequency:

$$\mathcal{E}(x,t) = E_c \cdot E(x,t)\,\frac{1}{\sqrt{L}} e^{i(n_{\mathrm{R}}\Omega/c)x} e^{-i\Omega t} \tag{A1a}$$

$$\mathcal{P}(x,t) = P_c \cdot P(x,t)\,\frac{1}{\sqrt{L}} e^{i(n_{\mathrm{R}}\Omega/c)x} e^{-i\Omega t} \tag{A1b}$$

$$\mathcal{D}(x,t) = D_c \cdot D(x,t)\,. \tag{A1c}$$

Following the above ansätze, the primary transformation happens in the wave equation for the electric field, equation (1*a*):

$$\partial_x^2 E + \frac{i2n_{\mathrm{R}}\Omega}{c}\partial_x E + \frac{i2n_c^2\Omega}{c^2}\dot{E} + \frac{n_c^2 - n_{\mathrm{R}}^2}{n_c^2}\frac{\Omega^2}{c^2}E - \frac{n_c^2}{c^2}\ddot{E} = \mu_0\epsilon_0\ddot{P} - i2\mu_0\epsilon_0\Omega\dot{P} - \mu_0\epsilon_0\Omega^2 P \tag{A2}$$

where we have used the explicit forms of E_c, P_c as defined in equation (3). The slowly-varying envelope approximation relies on the fact that the spatio-temporal evolution of the envelope functions E, P will unfold at rates smaller than Ω and Ω/c. More precisely, this requires $(\Omega/c)\partial_x E \gg \partial_x^2 E$, $\Omega\dot{E} \gg \ddot{E}$, and with analogous conditions holding for the polarization field. Dropping these second-order derivatives, the electric field wave equation reduces to an advection equation of the form:

$$i\dot{E} = \left[-i\frac{n_{\mathrm{R}}}{n_c^2}c\,\partial_x - \frac{n_c^2 - n_{\mathrm{R}}^2}{n_c^2}\frac{\Omega}{2}\right]E - \frac{\Omega}{2n_c^2}P \tag{A3}$$

where we have also used $\mu_0\epsilon_0 = \frac{1}{c^2}$. Now recalling that $n_c = n_{\mathrm{R}} + in_{\mathrm{I}}$ where $\frac{n_{\mathrm{I}}}{n_{\mathrm{R}}} \ll 1$, we can write the two respective contributions above to lowest nontrivial order in $\frac{n_{\mathrm{I}}}{n_{\mathrm{R}}}$:

$$\begin{aligned}\frac{n_{\mathrm{R}}}{n_c^2} &= \frac{1}{n_{\mathrm{R}}}\left(1 + i\frac{n_{\mathrm{I}}}{n_{\mathrm{R}}}\right)^{-2} \simeq \frac{1}{n_{\mathrm{R}}} - i\frac{2n_{\mathrm{I}}}{n_{\mathrm{R}}^2}\\ \frac{n_c^2 - n_{\mathrm{R}}^2}{n_c^2} &= 1 - \left(1 + i\frac{n_{\mathrm{I}}}{n_{\mathrm{R}}}\right)^{-2} \simeq i\frac{2n_{\mathrm{I}}}{n_{\mathrm{R}}}.\end{aligned} \tag{A4}$$

Using these results allows us to write the advection equation to lowest nontrivial order in $\frac{n_{\mathrm{I}}}{n_{\mathrm{R}}}$,

$$i\dot{E} = \left[-i\frac{c}{n_{\mathrm{R}}}\,\partial_x E - \frac{2n_{\mathrm{I}}}{n_{\mathrm{R}}^2}\,c\,\partial_x E - i\frac{2n_{\mathrm{I}}}{n_{\mathrm{R}}}\cdot\frac{\Omega}{2}\right]E - \frac{\Omega}{2n_c^2}P. \tag{A5}$$

If we now define the cold cavity loss rate as

$$\kappa \equiv \left(\frac{n_{\mathrm{I}}}{n_{\mathrm{R}}}\right)\Omega, \tag{A6}$$

we finally obtain:

$$\dot{E} = -\frac{c}{n_{\mathrm{R}}}\left(1 - i\frac{2n_{\mathrm{I}}}{n_{\mathrm{R}}}\right)\partial_x E - \kappa E + i\frac{\Omega}{2n_{\mathrm{R}}^2}P. \tag{A7}$$

Finally, using equation (5), the above equation can be expressed in dimensionless form:

$$\dot{E} = -\frac{1}{n_{\mathrm{R}}}\left(1 - i\frac{2n_{\mathrm{I}}}{n_{\mathrm{R}}}\right)\partial_x E - \kappa E + i\frac{\Omega}{2n_{\mathrm{R}}^2}P. \tag{A8}$$

Next, we substitute the ansätze into equation (1*b*) and simplify, which yields:

$$\dot{P} = -\gamma_\perp P - i\gamma_\perp E D. \tag{A9}$$

Finally, substituting the ansätze into equation (1*c*) and simplifying using equation (5), we obtain:

$$\dot{D} = -\gamma_{\parallel}\left(D - D^{0}\right) + i\frac{\gamma_{\parallel}}{2}\left(EP^{*} - E^{*}P\right). \tag{A10}$$

Appendix B. Review of main results of the spatiotemoral LSA

For completeness, we present here the results of the original spatiotemporal (ST) LSA from [32], in the notation of the main text. This LSA predicts minimum and maximum unstable frequencies at any pump power p given respectively by:

$$\omega_{\mathrm{max,min}} = \sqrt{\frac{\gamma_{\parallel}}{2}\left(3\gamma_{\perp}\left(p-1\right) - \gamma_{\parallel} \pm R\right)} \times \left(1 - \frac{2\kappa}{\gamma_{\perp}\left(p-3\right) - \gamma_{\parallel} \pm R}\right) \tag{B1}$$

where:

$$R = \sqrt{\gamma_{\perp}^{2}\left(p-1\right)^{2} - 2\gamma_{\perp}\left(p-1\right)\left(4\gamma_{\perp} + 3\gamma_{\parallel}\right) + \gamma_{\parallel}^{2}}. \tag{B2}$$

We define as ω_{inst} the value of the unstable frequency at the emergence of the instability of single mode lasing. Here $\omega_{\mathrm{max}} = \omega_{\mathrm{min}}$, and hence $R = 0$. This also provides the value of the pump power threshold for the instability:

$$p_{\mathrm{th}} = 5 + 3\left(\frac{\gamma_{\parallel}}{\gamma_{\perp}}\right) + 2\sqrt{4 + 6\left(\frac{\gamma_{\parallel}}{\gamma_{\perp}}\right) + 2\left(\frac{\gamma_{\parallel}}{\gamma_{\perp}}\right)^{2}}. \tag{B3}$$

To lowest order in $\frac{\gamma_{\parallel}}{\gamma_{\perp}}$, we recover the often-quoted value for the second thresold, $p_{\mathrm{th}} \to 9$. We note that this is only true in the large $\gamma_{\perp}$ limit.

Defining $\Delta_{\mathrm{inst}} = \omega_{\mathrm{max}} - \omega_{\mathrm{min}}$, considering the near threshold regime, we present results to lowest order in $\frac{\kappa}{\gamma_{\perp}}, \frac{\gamma_{\parallel}}{\gamma_{\perp}}$ are presented in equations (19*a*) and (19*b*).

The unstable frequency ω_{inst} can become zero under specific circumstances. Requiring $\omega_{\mathrm{inst}} = 0$ using equation (B1), we find that this condition is met at a pump power p given by:

$$p\left(\omega_{\mathrm{inst}} = 0\right) = \frac{\kappa}{\gamma_{\perp}} \cdot \frac{\gamma_{\parallel} + 3\gamma_{\perp} + \kappa}{\kappa - \gamma_{\parallel} - \gamma_{\perp}}. \tag{B4}$$

Clearly for this pump power to be positive and hence physical, we require:

$$\kappa > \gamma_{\parallel} + \gamma_{\perp} \tag{B5}$$

which is the 'bad cavity' limit of laser operation.

Appendix C. Modes of a lossy multimode ring cavity: non-Hermitian boundary value problem

In this appendix section we will determine the appropriate modes that define a lossy, effectively one-dimensional multimode ring cavity under the assumption of the absence of radial leakage. This will require solving both equations (6) and (7) from the main text.

The need for a separation of right and left eigenmodes is enforced by the non-Hermiticity of the operator $\mathcal{H}$ introduced in equation (6). We therefore quickly prove this feature of $\mathcal{H}$. Doing so requires defining an inner product on the function space where $\mathcal{H}$ operates:

$$\langle f|g\rangle \equiv \int_{0}^{1} \mathrm{d}x\, f^{*}\left(x\right) g\left(x\right). \tag{C1}$$

Then, if $\mathcal{H}$ is a Hermitian operator, it must satisfy $\langle f|\mathcal{H}g\rangle = \langle \mathcal{H}f|g\rangle$ [65] for generic functions with some boundary conditions; here, we consider periodic boundary conditions $f(x+1) = f(x)$ relevant for ring

cavities. To determine whether this is the case, we expand the former quantity, making use of integration-by-parts:

$$\begin{aligned}\langle f|\mathcal{H}g\rangle &= \int_0^1 \mathrm{d}x\, f^*\left[-\frac{1}{n_c^2}\frac{d^2 g}{\mathrm{d}x^2}\right]\\ &= -\frac{1}{n_c^2}\underbrace{\left[f^*\frac{\mathrm{d}g}{\mathrm{d}x}\right]_{x=0}^{x=1}}_{=0} + \frac{1}{n_c^2}\int_0^1 \mathrm{d}x\,\frac{\mathrm{d}f^*}{\mathrm{d}x}\frac{\mathrm{d}g}{\mathrm{d}x}\\ &= \frac{1}{n_c^2}\underbrace{\left[\frac{\mathrm{d}f^*}{\mathrm{d}x}g\right]_{x=0}^{x=1}}_{=0} - \frac{1}{n_c^2}\int_0^1 \mathrm{d}x\,\frac{d^2 f^*}{\mathrm{d}x^2}g\\ &= \int_0^1 \mathrm{d}x\,\left[-\frac{1}{n_c^2}\frac{d^2 f^*}{\mathrm{d}x^2}\right]g(x)\\ &= \int_0^1 \mathrm{d}x\,\left[-\frac{1}{n_c^{*2}}\frac{d^2 f}{\mathrm{d}x^2}\right]^* g(x) = \int_0^1 \mathrm{d}x\,\left(\mathcal{H}^* f\right)^* g(x)\\ &= \langle \mathcal{H}^* f|g\rangle \neq \langle \mathcal{H}f|g\rangle. \end{aligned} \tag{C2}$$

Note that boundary terms vanish due to the constraints on functions f, g. Clearly, $\mathcal{H}$ is non-Hermitian, since $n_c \neq n_c^*$, which requires the inroduction of $\mathcal{H}^*$.

We can now proceed with analyzing the right eigenmodes of $\mathcal{H}$, defined via equation (6) and reproduced below for the one-dimensional ring cavity and in dimensionless units as defined by equation (5):

$$\mathcal{H}\varphi_m(x) \equiv -\frac{1}{n_c^2}\frac{d^2}{\mathrm{d}x^2}\varphi_m(x) = \omega_m^2\varphi_m(x). \tag{C3}$$

The above Helmholtz equation can be solved by assuming ansätze for the mode functions $\varphi_m(x)$ of the form:

$$\varphi_m(x) = Ne^{ik_m x} \tag{C4}$$

where k_m is a dimensionless wavevector, and N is a normalization constant. Note that for equation (C4) to satisfy the Helmholtz equation for the ring cavity, it must satisfy periodic boundary conditions, so that:

$$e^{ik_m x} = e^{ik_m(x+1)} \implies k_m = 2m\pi,\ m \in \mathbb{Z}. \tag{C5}$$

Substituting the above and simplifying, we obtain the relation:

$$\left[-\frac{k_m^2}{n_c^2} + \omega_m^2\right]\varphi_m(x) = 0. \tag{C6}$$

The above immediately yields the dispersion relation:

$$\omega_m = \frac{1}{n_c}k_m. \tag{C7}$$

Recalling that n_c is complex-valued, the eigenfrequencies ω_m must also be complex, and describe the decay of field intensity for the lossy ring cavity modes (in the absence of pumping and subsequent lasing).

$$\begin{aligned}\omega_m &= \frac{1}{n_\mathrm{R} + in_\mathrm{I}}k_m\\ &\simeq \frac{k_m}{n_\mathrm{R}} - i\frac{k_m}{n_\mathrm{R}}\frac{n_\mathrm{I}}{n_\mathrm{R}} \equiv \nu_m - i\kappa_m. \end{aligned} \tag{C8}$$

Recalling that we have chosen parameters such that $\nu_0 = \Omega$, we find:

$$\nu_0 = \frac{k_0}{n_\mathrm{R}} = \Omega,\ \kappa_0 = \frac{k_0}{n_\mathrm{R}}\frac{n_\mathrm{I}}{n_\mathrm{R}} = \Omega\frac{n_\mathrm{I}}{n_\mathrm{R}} = \kappa. \tag{C9}$$

However, the spectrum of the non-Hermitian operator $\mathcal{H}$ is not fully defined without also obtaining the 'left' eigenmodes; these are obtained by solving the dual eigenproblem of the adjoint $\mathcal{H}^*$,

$$\mathcal{H}^*\widetilde{\varphi}_m(x) = -\frac{1}{n^{*2}}\frac{d^2}{\mathrm{d}x^2}\widetilde{\varphi}_m(x) = \widetilde{\omega}_m^2\widetilde{\varphi}_m(x). \tag{C10}$$

The dual functions $\{\widetilde{\varphi}_m\}$ are the left eigenmodes of the adjoint operator $\mathcal{H}^*$, here with eigenvalues $\widetilde{\omega}_m^2$. Note that this eigenvalue problem is in the form of another Helmholtz equation, and therefore can be solved very similarly to equation (C3). We assume the ansatz:

$$\widetilde{\varphi}_m(x) = \widetilde{N} e^{i\widetilde{k}_m x}. \tag{C11}$$

While *a priori* $\widetilde{k}_m$ are distinct from k_m, the left eigenmodes satisfy the same boundary conditions as the right eigenmodes for the case of a ring cavity, so that we have $\widetilde{k}_m = 2m\pi = k_m$.

Substituting the above ansatz into equation (C10), we quickly arrive at the relation

$$\left[-\frac{\widetilde{k}_m^2}{n_c^{*2}} + \widetilde{\omega}_m^2\right]\widetilde{\varphi}_m(x) = 0 \tag{C12}$$

which immediately implies

$$\widetilde{\omega}_m = \nu_m + i\kappa_m = \omega_m^*. \tag{C13}$$

Hence the eigenvalues of the dual eigenproblem equal exactly the conjugates of the eigenvalues of the original eigenproblem, as has been found in earlier works [52].

It can be shown [52, 75] that the left and right eigenmodes together define the generalized orthogonality relationship for non-Hermitian operators such as $\mathcal{H}$, introduced in equation (8),

$$\int_0^1 dx\, \widetilde{\varphi}_m^*(x)\,\varphi_n(x) = \delta_{mn} \tag{C14}$$

which can easily be verified using the forms of the right and left eigenmodes already found.

For $n = m$, imposing the orthogonality relationship in equation (8), we can set $N = \widetilde{N} = \frac{1}{\sqrt{L}}$, so that the final expression for lossy right eigenmodes - returning to dimensionful units - takes the form:

$$\varphi_m(x) = \frac{1}{\sqrt{L}} e^{ik_m x},\ k_m L = 2m\pi,\ m \in \mathbb{Z} \tag{C15}$$

with complex eigenfrequencies ω_m given by equation (C8). Since $\widetilde{\omega}_m = \omega_m^*$, we do not need to keep track of the eigenvalues of the adjoint eigenproblem explicitly.

Appendix D. Derivation of CFTD equations

We will derive here equation (13) starting with the MBEs for the scalar electric field amplitude $E(x,t)$, polarization $P(x,t)$ and inversion density $D(x,t)$, equations (1*a*)–(1*c*). The procedure for obtaining the CFTD equations can be summarized as follows: we substitute the CF ansätze, equations (11*a*) and (11*b*) into each of the MBEs, integrate out the spatial component by taking advantage of properties of the CF states, and apply the slowly varying envelope approximation to eliminate second-order time derivatives.

Beginning by substituting equations (11*a*) and (11*b*) into equation (1*a*), we obtain (replacing $m \to n$ as the summation index):

$$\sum_n \left[\frac{E_n}{E_c}\nabla^2 - \frac{n_c^2}{c^2}\frac{\ddot{E}_n - i2\Omega\dot{E}_n - \Omega^2 E_n}{E_c}\right] e^{-i\Omega t}\varphi_n(x) = \mu_0 \sum_n \frac{\ddot{P}_n - i2\Omega\dot{P}_n - \Omega^2 P_n}{P_c} e^{-i\Omega t}\varphi_n(x). \tag{D1}$$

Using equation (6) the above simplifies to:

$$\sum_n \left[-\frac{n_c^2}{c^2}\frac{\omega_n^2 E_n}{E_c} - \frac{n_c^2}{c^2}\frac{\ddot{E}_n - i2\Omega\dot{E}_n - \Omega^2 E_n}{E_c}\right] e^{-i\Omega t}\varphi_n(x) = \mu_0 \sum_n \frac{\ddot{P}_n - i2\Omega\dot{P}_n - \Omega^2 P_n}{P_c} e^{-i\Omega t}\varphi_n(x). \tag{D2}$$

We are now able to make use of the generalized orthogonality relation, equation (8). Multiplying through by $\widetilde{\varphi}_m^*(x)$ and integrating over the spatial domain of the cavity, we find:

$$\sum_m \left[-\frac{n_c^2}{c^2}\frac{\omega_n^2 E_n}{E_c} - \frac{n_c^2}{c^2}\frac{\ddot{E}_n - i2\Omega\dot{E}_n - \Omega^2 E_n}{E_c} \right] e^{-i\Omega t} \times \int dx\, \widetilde{\varphi}_m^*(x)\,\varphi_n(x) = \mu_0 \sum_n \frac{\ddot{P}_n - i2\Omega\dot{P}_n - \Omega^2 P_n}{P_c} e^{-i\Omega t} \int dx\, \widetilde{\varphi}_m^*(x)\,\varphi_n(x). \tag{D3}$$

This spatial projection enables us to make use of the generelized orthogonality of the right eigenmodes $\{\varphi_m(x)\}$ and the left eigenmodes of the adjoint operator, $\{\widetilde{\varphi}_m(x)\}$, equation (8); this collapses the sum over modes, finally yielding:

$$\left[-\frac{n_c^2}{c^2}\frac{\omega_m^2 E_m}{E_c} - \frac{n_c^2}{c^2}\frac{\ddot{E}_m - i2\Omega\dot{E}_m - \Omega^2 E_m}{E_c} \right] e^{-i\Omega t} = \mu_0 \frac{\ddot{P}_m - i2\Omega\dot{P}_m - \Omega^2 P_m}{P_c} e^{-i\Omega t}. \tag{D4}$$

We now also perform a slowly-varying envelope approximation to neglect second-order time derivatives as before, namely $\ddot{E}_m \ll \Omega\dot{E}_m$ and $\ddot{P}_m \ll \Omega\dot{P}_m \ll \Omega^2 P_m$. Also making use of the explicit form of scaling factors E_c, P_c and rearranging terms, we arrive at:

$$-i2\Omega\dot{E}_m - \Omega^2 E_m + \omega_m^2 E_m = \frac{\Omega^2 \mu_0 \epsilon_0 c^2}{n_c^2} P_m. \tag{D5}$$

We will now introduce some replacements and a final set of approximations. Using $\mu_0\epsilon_0 = \frac{1}{c^2}$, $\omega_m^2 = \nu_m^2 - \kappa_m^2 - 2i\nu_m\kappa_m$, and approximating $\frac{\nu_m}{\Omega} \simeq 1$, $n_c \simeq n_{\mathrm{R}}(1 + i\frac{n_{\mathrm{I}}}{n_{\mathrm{R}}}) \simeq n_{\mathrm{R}}$, and scaling time and frequency scales according to equation (5), we arrive at the dynamical equation for the electric field amplitude of the nth mode is given by:

$$\dot{E}_m = \frac{i}{2\Omega}\left(\Omega^2 - \nu_m^2 + \kappa_m^2\right) E_m - \kappa_m E_m + \frac{i\Omega}{2n_{\mathrm{R}}^2} P_m \tag{D6}$$

which is equation (13*a*) from the main text.

Similarly substituting equations (11*a*) and (11*b*), into the dynamical equation for the polarization field, equation (1*b*), we obtain:

$$\sum_n \left[-i\Omega P_n + \dot{P}_n\right]\varphi_n(x) = \sum_n (-i\Omega - \gamma_\perp) P_n \varphi_n(x) - i\frac{g^2}{\hbar}\frac{P_c}{E_c D_c}\sum_n E_n D(x,t)\,\varphi_n(x). \tag{D7}$$

Once more multiplying through by $\widetilde{\varphi}_m^*(x)$, integrating over the spatial domain of the cavity, and using equation (8), we find:

$$\dot{P}_m = -\gamma_\perp P_m - i\gamma_\perp \sum_n E_n \widetilde{\varphi}_m^*(x) D(x,t)\,\varphi_n(x) \tag{D8}$$

where we have also used the explicit forms of E_c, P_c, and D_c. The term in brackets on the right defines the inversion matrix elements introduced in equation (12). Introducing these matrix elements, the equation of motion for the polarization field expansion coefficients is given by:

$$\dot{P}_m = -\gamma_\perp P_m - i\gamma_\perp \sum_n E_n D_{mn}. \tag{D9}$$

Finally, substituting equations (11*a*) and (11*b*), into the dynamical equation for the inversion field, equation (1*b*), we obtain:

$$\dot{D} = -\gamma_\parallel\left(D - D^0\right) + i\frac{2}{\hbar E_c P_c}\sum_{rs}\left[E_r P_s^* \varphi_r(x)\,\varphi_s^*(x) - E_r^* P_s \varphi_r^*(x)\,\varphi_s(x)\right]. \tag{D10}$$

Multiplying through by the scaling factor D_c, and re-ordering the sum by a redefinition of labels, we obtain:

$$\dot{D} = -\gamma_\parallel\left(D - D^0\right) + i\frac{2D_c}{\hbar E_c P_c}\sum_{rs}\left(E_r P_s^* - E_s^* P_r\right)\varphi_r(x)\,\varphi_s^*(x). \tag{D11}$$

We can now project the inversion field onto the spatial basis. We multiply through by $\widetilde{\varphi}_m^*(x)\varphi_n(x)$ and integrate over the spatial domain of the laser cavity, finally arriving at:

$$\dot{D}_{mn} = -\gamma_{\parallel}\left(D_{mn} - D_{mn}^0\right) + i\frac{\gamma_{\parallel}}{2}\sum_{rs}\mathcal{A}_{mrsn}\left(E_r P_s^* - E_r^* P_s\right) \tag{D12}$$

where we have used the explicit forms of the scaling factors, moved to dimensionless time and frequency variables, and introduced the dimensionless mode overlap tensor of the main text, equation (14):

$$\mathcal{A}_{mrsn} = \int_0^1 dx\, \widetilde{\varphi}_m^*\varphi_r\varphi_s^*\varphi_n. \tag{D13}$$

Using the explicit form of the mode overlap tensor, the equations of motion for the inversion matrix elements D_{mn} are finally given by:

$$\dot{D}_{mn} = -\gamma_{\parallel}\left(D_{mn} - D_{mn}^0\right) + \frac{i\gamma_{\parallel}}{2}\sum_{r}\left[E_r P_{n+r-m}^* - E_{n+r-m}^* P_r\right] \tag{D14}$$

Appendix E. Derivation of the single mode threshold

In this appendix section, we derive the pump threshold and steady-state lasing solution in the regime of single-mode lasing. We allow for a general lasing frequency Ω_l:

$$\begin{aligned} E_l(t) &= E_{\mathrm{ss}} e^{-i\Omega_l t} \\ P_l(t) &= P_{\mathrm{ss}} e^{-i\Omega_l t} \\ D_{ll}(t) &= D_{\mathrm{ss}} \end{aligned} \tag{E1}$$

where the inversion is stationary. Under this ansätz, the modal equations then simplify to:

$$\dot{E}_{\mathrm{ss}} = \frac{i}{2\Omega}\left(2\Omega\Omega_l + \Omega^2 - \nu_l^2 + \kappa_l^2\right)E_{\mathrm{ss}} - \kappa_0 E_{\mathrm{ss}} + \frac{i\Omega}{2n_{\mathrm{R}}^2}P_{\mathrm{ss}} \tag{E2a}$$

$$\dot{P}_{\mathrm{ss}} = \left(i\Omega_l - \gamma_{\perp}\right)P_{\mathrm{ss}} - i\gamma_{\perp}E_{\mathrm{ss}}D_{\mathrm{ss}} \tag{E2b}$$

$$\dot{D}_{\mathrm{ss}} = -\gamma_{\parallel}\left(D_{\mathrm{ss}} - D_{00}^0\right) + \frac{i\gamma_{\parallel}}{2}\left(E_{\mathrm{ss}}P_{\mathrm{ss}}^* - E_{\mathrm{ss}}^* P_{\mathrm{ss}}\right) \tag{E2c}$$

For steady-state, we require $\dot{E}_{\mathrm{ss}} = \dot{P}_{\mathrm{ss}} = \dot{D}_{\mathrm{ss}} = 0$. In this regime, equation (E2*a*) reduces to:

$$P_{\mathrm{ss}} = \left[-i\frac{2n_{\mathrm{R}}^2\kappa}{\Omega} - \frac{n_{\mathrm{R}}^2}{\Omega^2}\left(2\Omega\Omega_l + \Omega^2 - \nu_l^2 + \kappa_l^2\right)\right]E_{\mathrm{ss}}. \tag{E3}$$

Similarly, equation (E2*b*) yields for the same quantity:

$$P_{\mathrm{ss}} = \frac{i\gamma_{\perp}}{i\Omega_l - \gamma_{\perp}}\cdot E_{\mathrm{ss}}D_{\mathrm{ss}}. \tag{E4}$$

Comparing the two equations, we immediately find for D_{ss}:

$$\frac{i\gamma_{\perp}}{i\Omega_l - \gamma_{\perp}}\cdot D_{\mathrm{ss}} = \left[-i\frac{2n_{\mathrm{R}}^2\kappa_l}{\Omega} - \frac{n_{\mathrm{R}}^2}{\Omega^2}\left(2\Omega\Omega_l + \Omega^2 - \nu_l^2 + \kappa_l^2\right)\right] \tag{E5}$$

Or, rationalizing the left-hand side:

$$\frac{\Omega_l\gamma_{\perp} - i\gamma_{\perp}^2}{\Omega_l^2 + \gamma_{\perp}^2}D_{\mathrm{ss}} = \left[-i\frac{2n_{\mathrm{R}}^2\kappa_l}{\Omega} - \frac{n_{\mathrm{R}}^2}{\Omega^2}\left(2\Omega\Omega_l + \Omega^2 - \nu_l^2 + \kappa_l^2\right)\right]. \tag{E6}$$

Comparing both sides, the imaginary parts immediately yield:

$$D_{\mathrm{ss}} = \frac{\Omega_l^2 + \gamma_{\perp}^2}{\gamma_{\perp}^2}\frac{2n_{\mathrm{R}}^2\kappa_l}{\Omega} \tag{E7}$$

while the real parts yield:

$$\frac{\Omega_l\gamma_\perp}{\Omega_l^2+\gamma_\perp^2}D_{\rm ss} = -\left[\frac{n_{\rm R}^2}{\Omega^2}\left(2\Omega\Omega_l+\Omega^2-\nu_l^2+\kappa_l^2\right)\right]. \tag{E8}$$

Substituting the expression for $D_{\rm ss}$ into the above, we immediately find:

$$\frac{\Omega_l}{\gamma_\perp}\frac{2n_{\rm R}^2\kappa_l}{\Omega} = -\left[\frac{n_{\rm R}^2}{\Omega^2}\left(2\Omega\Omega_l+\Omega^2-\nu_l^2+\kappa_l^2\right)\right] \tag{E9}$$

which finally yields:

$$\frac{2n_{\rm R}^2}{\Omega}\left(\frac{\kappa_l}{\gamma_\perp}+1\right)\Omega_l = -\frac{n_{\rm R}^2}{\Omega^2}\left(\Omega^2-\nu_l^2+\kappa_l^2\right) \tag{E10}$$

or:

$$\left(\frac{\kappa_l}{\gamma_\perp}+1\right)\Omega_l = -\frac{\left(\Omega^2-\nu_l^2+\kappa_l^2\right)}{\Omega}. \tag{E11}$$

Finally, using equation (E2*c*) we find:

$$0 = -\gamma_\parallel\left(D_{\rm ss}-D_{00}^0\right)+\frac{i\gamma_\parallel}{2}\left(\frac{i\gamma_\perp}{i\Omega_l+\gamma_\perp}-\frac{i\gamma_\perp}{i\Omega_l-\gamma_\perp}\right)D_{\rm ss}|E_{\rm ss}|^2 \tag{E12}$$

which simplifies to:

$$\begin{aligned} D_{\rm ss} &= D_{00}^0-\left(\frac{\gamma_\perp^2}{\Omega_l^2+\gamma_\perp^2}\right)D_{\rm ss}|E_{\rm ss}|^2 \\ \implies D_{\rm ss} &= \frac{D_{00}^0}{1+\frac{\gamma_\perp^2}{\Omega_l^2+\gamma_\perp^2}|E_{\rm ss}|^2}. \end{aligned} \tag{E13}$$

Using equation (E7), we can solve for $E_{\rm ss}$:

$$\left(\frac{\Omega_l^2+\gamma_\perp^2}{\gamma_\perp^2}+|E_{\rm ss}|^2\right)\frac{2n_{\rm R}^2\kappa_l}{\Omega} = D_{00}^0 \tag{E14}$$

which can be rewritten in the form:

$$|E_{\rm ss}|^2 = \frac{\Omega}{2n_{\rm R}^2\kappa_l}D_{00}^0-\frac{\Omega_l^2+\gamma_\perp^2}{\gamma_\perp^2}. \tag{E15}$$

The requirement of $|E_{\rm ss}|^2>0$ yields:

$$D_{00}^0 \geq \frac{2n_{\rm R}^2\kappa_l}{\Omega}\cdot\frac{\Omega_l^2+\gamma_\perp^2}{\gamma_\perp^2} \tag{E16}$$

which yields the single-mode lasing threshold $D_{\rm th}$:

$$D_{\rm th} = \frac{2n_{\rm R}^2\kappa_l}{\Omega}\cdot\frac{\Omega_l^2+\gamma_\perp^2}{\gamma_\perp^2} \tag{E17}$$

Clearly minimizing this threshold for fixed damping parameters requires minimizing κ_l and Ω_l. Assuming all modes have equal damping rates $\kappa_l=\kappa\ \forall\ l$, the lasing threshold is minimized for mode l that minimizes Ω_l. From equation (E11), $\Omega_l=0$ if $\left(\Omega^2-\nu_l^2+\kappa_l^2\right)=0$, which requires:

$$\nu_l^2 = \left(\Omega^2+\kappa_l^2\right) \implies \nu_l\simeq\Omega \tag{E18}$$

as $\kappa_l\ll\Omega$. Namely, the mode l closest to the atomic transition frequency will have the lowest single-mode lasing threshold.

Appendix F. Details of the multimode LSA

To analyze the linear stability of single-mode lasing dynamics described by the CFTD equations, we substitute the ansätze of equation (20*c*) into equations (13*a*)–(13*c*), and retain only terms linear in the fluctuation variables $(\delta E_m, \delta P_m, \delta D_{mn})$. Under this linearization, the equation of motion for the electric field amplitudes, which is already linear, retains its form and is given by equation (13*a*):

$$\delta\dot{E}_m = \frac{i}{2\Omega}\left(\Omega^2 - \nu_m^2 + \kappa_m^2\right)\delta E_m - \kappa_m \delta E_m + \frac{i\Omega}{2n_R^2}\delta P_m \tag{F1}$$

while the equation of motion for polarization field, equation (13*b*), for sidebands $m \neq 0$ take the form:

$$\delta\dot{P}_m = -\gamma_\perp \delta P_m - i\gamma_\perp \left[E_0 \delta D_{m0} + \sum_{l\neq 0} \delta E_l D_{00}\delta_{ml}\right] \tag{F2}$$

where we have dropped terms involving the product of two fluctuation terms $\sim O(\delta E_m \delta D_{ml}), m \neq 0$ in the second line. It is clear that the nontrivial inversion matrix elements that couple to the emerging sidebands are off-diagonal elements namely D_{m0}. Using equation (13*c*), we can write equations of motion for these inversion matrix elements:

$$\delta\dot{D}_{m0} = -\gamma_\parallel\left(\delta D_{m0} - D^0_{m0}\right) + \frac{i\gamma_\parallel}{2}\left[E_0\delta P^*_m + \delta E_{-m}P^*_0 - \delta E^*_m P_0 - E^*_0 \delta P_{-m}\right] \tag{F3}$$

where we have now dropped second-order terms such as $O(\delta E_r \delta P_{m+r}), r \neq 0, -m$.

Equations (F1)–(F3) can be compactly written in matrix form, yielding the matrix system in equation (21) of the main text. The component matrices are given by:

$$\mathbf{J}_m = \begin{pmatrix} \frac{i\left(\Omega^2+\kappa_m^2-\nu_m^2\right)-2\kappa_m\Omega}{\Omega} & 0 & \frac{i\Omega}{2n_c^2} & 0 & 0 & 0 \\ 0 & \frac{i\left(\Omega^2+\kappa_m^2-\nu_m^2\right)-2\kappa_m\Omega}{\Omega} & -\frac{i\Omega}{2n_c^2} & 0 & 0 & \\ -iD_{00}\gamma_\perp & 0 & -\gamma_\perp & 0 & -iE_0\gamma_\perp & 0 \\ 0 & iD_{00}\gamma_\perp & 0 & -\gamma_\perp & 0 & iE_0^*\gamma_\perp \\ \frac{i}{2}\gamma_\parallel P_0^* & 0 & -\frac{i}{2}\gamma_\parallel E_0^* & 0 & -\gamma_\parallel & 0 \\ 0 & -\frac{i}{2}\gamma_\parallel P_0 & 0 & \frac{i}{2}\gamma_\parallel E_0 & 0 & -\gamma_\parallel \end{pmatrix}. \tag{F4}$$

The dependence on mode index m arises only via the electric field sector. The coupling matrices $\mathbf{C}_{m,-m}$ are symmetric under $m \to -m$ are given by:

$$\mathbf{C}_{m,-m} = \begin{pmatrix} 0 & 0 & 0 & 0 & 0 & 0 \\ 0 & 0 & 0 & 0 & 0 & 0 \\ 0 & 0 & 0 & 0 & 0 & 0 \\ 0 & 0 & 0 & 0 & 0 & 0 \\ 0 & -\frac{i}{2}\gamma_\parallel P_0 & 0 & \frac{i}{2}\gamma_\parallel E_0 & 0 & 0 \\ \frac{i}{2}\gamma_\parallel P_0^* & 0 & -\frac{i}{2}\gamma_\parallel E_0^* & 0 & 0 & 0 \end{pmatrix}. \tag{F5}$$

The coupling matrix has a sparse form, and clearly emphasizes that sideband coupling arises via the inversion field sector of the dynamics (the final two rows).

Appendix G. Additional numerical results

In this section we provide some additional simulation results that supplement discussions in the main text regarding the comparison of the two methods as well as other features of the CFTD.

G.1. An intermediate polarization regime: $\gamma_\perp/\gamma_\parallel = 10.0$

We consider here an additional intermediate ratio $\gamma_\perp/\gamma_\parallel = 10$ as shown in figure 10. The decay parameters are: $\gamma_\perp = 5, \gamma_\parallel = 0.5$ and $\kappa = 0.1$. The ST LSA reveals that the first mode pair to become unstable is at the frequencies $\Omega \pm 2\Delta$. As we have previously seen, we can extract the unstable modes by looking at the intersection of each pump power and the instability band shaded in pink. The black circles in the same figure mark the modal linear stability results. The two analyses begin to diverge here for higher pump power as the modal approach seems to predict a smaller range of instability than the RNGH analysis.

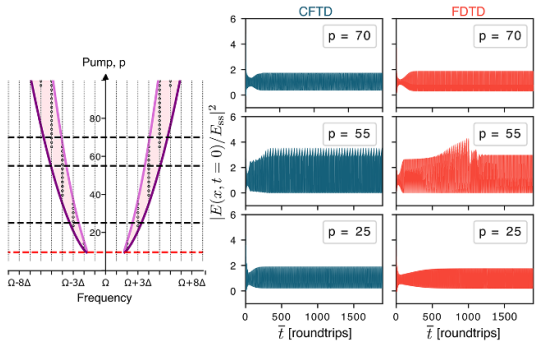

Figure 10. CFTD and FDTD comparison for decay parameters: $\gamma_\perp = 5.0, \gamma_\parallel = 0.5, \kappa = 0.1$, and $n_R = 1.96$. Left panel: ST LSA where red dashed line marks the instability threshold and black dashed lines mark pump powers where time traces are shown. Regions marked by black open circles show the results of the modal LSA. Right panel: Side by side comparison of $|E(x = 0, t)|^2$ scaled by E_{ss} for the first 2000 roundtrips of the CFTD (blue) and FDTD (red) results.

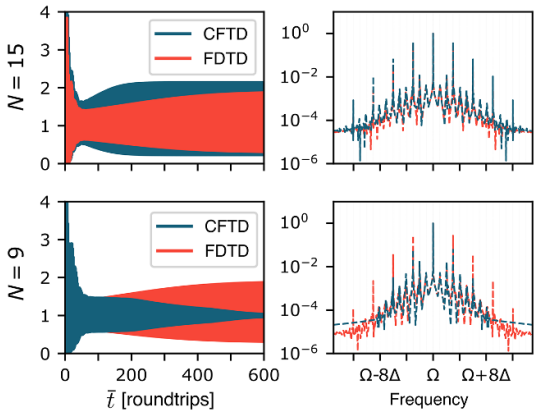

Figure 11. Comparison of dynamics of the scaled electric field intensity $|E(x = 0, t)|^2$ and its FFT using CFTD (blue) and FDTD (red), above the instability threshold ($p = 25$) for two different numbers of modes included in the CFTD simulation. Decay parameters are $\gamma_\perp = 5.0, \gamma_\parallel = 0.5, \kappa = 0.1$, and $n_R = 1.96$.

In this case, we show numerical CFTD and FDTD simulations for pump powers $p = 25$ and $p = 70$. In these cases only a single mode becomes unstable at frequencies $\Omega \pm 3\Delta$ and $\Omega \pm 5\Delta$ respectively. The time traces of the electric field computed using both CFTD and FDTD simulations show sustained oscillations in these cases, while the frequency spectra of the fields will reveal prominent peaks at the unstable mode pairs (not shown). However, this qualitative agreement is accompanied by certain discrepancies, such as the rate at which solutions reach steady state, and the steady-state oscillation amplitude.

The intermediate pump power result, $p = 55$, describes a special case: here, *two* mode pairs are simultaneously predicted to be unstable by the ST LSA ($\Omega \pm 4\Delta$ and $\Omega \pm 5\Delta$ fall simultaneously in the instability band). As seen in figure 5, for simpler instabilities with a single unstable seed mode pair, this mode number determines the FSR spacing of the emergent multimode comb. With two adjacent unstable mode pairs, the nature of the comb waveform is not *a priori* obvious, as the mode numbers are incompatible with a fixed FSR comb. The time domain electric field traces shown in figure 10 using both simulation methods reveal that the dynamics is more complex than the single mode pair case.

G.2. The role of the retained number of modes

As a modal approach, one of the main parameters in the CFTD simulations is the number of modes. Generally, a larger number of modes leads to greater accuracy as defined by the discrepancy with the FDTD solution; however, if the number of modes is too large, it will lead to a greater simulation time without any benefit in accuracy and may even give rise to artifacts. In our analysis in the main text, the choice of number of modes has been guided by two factors. First, in order to produce an initial pulse that closely resembles a Gaussian pulse, at least 11 modes have been included in each simulation regardless of the relevant number of modes in the system. For some of the regimes we have considered, this is a sufficient number of modes. The second factor we have consulted is the LSA by including at least enough modes to cover the instability bands. To highlight the importance of the number of modes, we have shown in figure 11(a) comparison of two

simulations where the difference lies only in the total number of modes included. The top panel shows the CFTD and FDTD time traces as well as spectra for a greater number of modes, in this case 15. We do see a discrepancy between the two methods in the time domain, where the FDTD is slower to reach the steady state oscillations. As we have analyzed in the main text, this parameter space belongs to a relatively complex regime, where the agreement between the two methods is more qualitative. However, the agreement over the modes present in each simulation is very good. In the bottom panel we show the same comparison between the two methods but now the number of modes included in the CFTD is only 9. The results are now qualitatively very different between the CFTD and FDTD where the CFTD settles to steady state and thus shows fewer modes to be present. In fact, the few sidebands that are present in the CFTD spectrum are due to the transient dynamics in the beginning of the time trace.

References

[1] Ge Li, Malik O and Türeci H E 2014 Enhancement of laser power-efficiency by control of spatial hole burning interactions *Nat. Photon.* **8** 871–5
[2] Aung N L, Ge Li, Malik O, Türeci H E and Gmachl C F 2015 Threshold current reduction and directional emission of deformed microdisk lasers via spatially selective electrical pumping *Appl. Phys. Lett.* **107** 151106
[3] Wang C Y *et al* 2007 Coherent instabilities in a semiconductor laser with fast gain recovery *Phys. Rev.* A **75** 031802
[4] Lugiato L A and Prati F 2019 Self-pulsing in Fabry-Perot lasers: an analytic scenario *Phys. Rev. Res.* **1** 032029
[5] Silvestri C, Luigi Columbo L, Brambilla M and Gioannini M 2020 Coherent multi-mode dynamics in a quantum cascade laser: amplitude- and frequency-modulated optical frequency combs *Opt. Express* **28** 23846–61
[6] Wang Y and Belyanin A 2020 Harmonic frequency combs in quantum cascade lasers: time-domain and frequency-domain theory *Phys. Rev.* A **102** 013519
[7] Vukovic N, Radovanovic J, Milanovic V and Boiko D L 2020 Numerical study of Risken-Nummedal-Graham-Haken instability in mid-infrared Fabry-Pérot quantum cascade lasers *Opt. Quantum Electron.* **52** 91
[8] Piccardo M and Capasso F 2021 Laser frequency combs with fast gain recovery: physics and applications *Laser Photon. Rev.* **16** 2100403
[9] Täschler P, Bertrand M, Schneider B, Singleton M, Jouy P, Kapsalidis F, Beck M and Faist J 2021 Femtosecond pulses from a mid-infrared quantum cascade laser *Nat. Photon.* **15** 919–24
[10] Mirian N S *et al* 2021 Generation and measurement of intense few-femtosecond superradiant extreme-ultraviolet free-electron laser pulses *Nat. Photon.* **15** 523–9
[11] Sugioka K 2017 Progress in ultrafast laser processing and future prospects *Nanophotonics* **6** 393–413
[12] Torre R, Bartolini P and Righini R 2004 Structural relaxation in supercooled water by time-resolved spectroscopy *Nature* **428** 296–9
[13] Huber R, Tauser F, Brodschelm A, Bichler M, Abstreiter G and Leitenstorfer A 2001 How many-particle interactions develop after ultrafast excitation of an electron–hole plasma *Nature* **414** 286–9
[14] Morgner U, Kärtner F X, Cho S H, Chen Y, Haus H A, Fujimoto J G, Ippen E P, Scheuer V, Angelow G and Tschudi T 1999 Sub-two-cycle pulses from a Kerr-lens mode-locked Ti:sapphire laser *Opt. Lett.* **24** 411–3
[15] Kim J and Song Y 2016 Ultralow-noise mode-locked fiber lasers and frequency combs: principles, status and applications *Adv. Opt. Photonics* **8** 465–540
[16] Revin D G, Hemingway M, Wang Y, Cockburn J W and Belyanin A 2016 Active mode locking of quantum cascade lasers in an external ring cavity *Nat. Commun.* **7** 11440
[17] Hillbrand J, Opačak N, Piccardo M, Schneider H, Strasser G, Capasso F and Schwarz B 2020 Mode-locked short pulses from an 8 μm wavelength semiconductor laser *Nat. Commun.* **11** 5788
[18] Kippenberg T J, Gaeta A L, Lipson M and Gorodetsky M L 2018 Dissipative Kerr solitons in optical microresonators *Science* **361** 6402
[19] Pfeiffer M H P, Herkommer C, Liu J, Guo H, Karpov M, Lucas E, Zervas M and Kippenberg T J 2017 Octave-spanning dissipative Kerr soliton frequency combs in Si_3N_4 microresonators *Optica* **4** 684–91
[20] Meng B, Singleton M, Hillbrand J, Franckié M, Beck M and Faist J 2022 Dissipative Kerr solitons in semiconductor ring lasers *Nat. Photon.* **16** 142–7
[21] Picqué N and Hänsch T W 2019 Frequency comb spectroscopy *Nat. Photon.* **13** 146–57
[22] Udem T, Holzwarth R and Hänsch T W 2002 Optical frequency metrology *Nature* **416** 233–7
[23] Lezius M *et al* 2016 Space-borne frequency comb metrology *Optica* **3** 1381–7
[24] Papp S B, Beha K, Del'Haye P, Quinlan F, Lee H, Vahala K J and Diddams S A 2014 Microresonator frequency comb optical clock *Optica* **1** 10–14
[25] Gaeta A L, Lipson M and Kippenberg T J 2019 Photonic-chip-based frequency combs *Nat. Photon.* **13** 158–69
[26] Lamb W E Jr 1964 Theory of an optical maser *Phys. Rev.* **134** A1429–50
[27] Hendow S T and Sargent M 1982 The role of population pulsations in single-mode laser instabilities *Opt. Commun.* **40** 385–90
[28] Hendow S T and Sargent M 1982 Effects of detuning on single-mode laser instabilities *Opt. Commun.* **43** 59–63
[29] Lugiato L A, Narducci L M, Bandy D K and Abraham N B 1983 Instabilities in inhomogeneously broadened single-mode lasers *Opt. Commun.* **46** 115–20
[30] Lugiato L A, Narducci L M, Eschenazi E V, Bandy D K and Abraham N B 1985 Multimode instabilities in a homogeneously broadened ring laser *Phys. Rev.* A **32** 1563–75
[31] Agrawal G P 1988 Population pulsations and nondegenerate four-wave mixing in semiconductor lasers and amplifiers *J. Opt. Soc. Am. B* **5** 147–59
[32] Risken H and Nummedal K 1968 Self-pulsing in lasers *J. Appl. Phys.* **39** 4662–72
[33] Graham R and Haken H 1968 Quantum theory of light propagation in a fluctuating laser-active medium *Z. Phys.* A **213** 420–50
[34] Mansuripur T S *et al* 2016 Single-mode instability in standing-wave lasers: the quantum cascade laser as a self-pumped parametric oscillator *Phys. Rev.* A **94** 063807
[35] Hillman L W, Krasiński J, Boyd R W and Stroud C R 1984 Observation of higher order dynamical states of a homogeneously broadened laser *Phys. Rev. Lett.* **52** 1605–8

[36] Hillman L W, Krasinski J, Koch K and Stroud C R 1985 Dynamics of homogeneously broadened lasers: higher-order bichromatic states of operation *J. Opt. Soc. Am. B* **2** 211–7
[37] Roldán E and de Valcárcel G J 1998 On the observability of the Risken-Nummedal-Graham-Haken multimode instability in erbium-doped fibre lasers *Europhys. Lett.* **43** 255–60
[38] Voigt T, Lenz M O, Mitschke F, Roldán E and de Valcárcel G J 2004 Experimental investigation of Risken-Nummedal-Graham-Haken laser instability in fiber ring lasers *Appl. Phys.* B **79** 175–83
[39] Hugi A, Villares G, Blaser S, Liu H C and Faist J 2012 Mid-infrared frequency comb based on a quantum cascade laser *Nature* **492** 229–33
[40] Piccardo M *et al* 2020 Frequency combs induced by phase turbulence *Nature* **582** 360–4
[41] Jaidl M *et al* 2021 Comb operation in terahertz quantum cascade ring lasers *Optica* **8** 780–7
[42] Vuković N N, Radovanović J, Milanović V and Boiko D L 2017 Low-threshold RNGH instabilities in quantum cascade lasers *IEEE J. Sel. Top. Quantum Electron.* **23** 1–16
[43] Demeter G 2013 Solving the Maxwell-Bloch equations for resonant nonlinear optics using GPUs *Comput. Phys. Commun.* **184** 1203–10
[44] Wang S, Docherty A, Marks B S and Menyuk C R 2013 Comparison of numerical methods for modeling laser mode locking with saturable gain *J. Opt. Soc. Am.* B **30** 3064
[45] Kirch J D, Chang C-C, Boyle C, Mawst L J, Lindberg D, Earles T and Botez D 2015 5.5 w near-diffraction-limited power from resonant leaky-wave coupled phase-locked arrays of quantum cascade lasers *Appl. Phys. Lett.* **106** 061113
[46] Liu Y-H, Zhang J-C, Yan F-L, Liu F-Q, Zhuo N, Wang Li-J, Liu J-Q and Wang Z-G 2015 Coupled ridge waveguide distributed feedback quantum cascade laser arrays *Appl. Phys. Lett.* **106** 142104
[47] Zhou W, Lu Q-Y, Wu D-H, Slivken S and Razeghi M 2019 High-power, continuous-wave, phase-locked quantum cascade laser arrays emitting at 8 μm *Opt. Express* **27** 15776–85
[48] Liu Y G N, Wei Y, Hemmatyar O, Pyrialakos G G, Jung P S, Christodoulides D N and Khajavikhan M 2022 Complex skin modes in non-Hermitian coupled laser arrays *Light: Sci. Appl.* **11** 336
[49] Kacmoli S, Sivco D L and Gmachl C F 2023 Photonic molecule based on coupled ring quantum cascade lasers *Optica* **10** 1210–6
[50] D'Alessandro G, Kent A J and Oppo G L 1996 Centre manifold reduction of laser equations with transverse effects: an approach based on modal expansion *Opt. Commun.* **131** 172–94
[51] de Valcárcel G J, Roldán E and Prati F 2003 Modal expansions in lasers outside the uniform-field limit *J. Opt. Soc. Am.* B **20** 825–30
[52] Ge Li, Chong Y D and Douglas Stone A 2010 Steady-state *ab initio* laser theory: generalizations and analytic results *Phys. Rev.* A **82** 063824
[53] Malik O, Makris K G and Türeci H E 2015 Spectral method for efficient computation of time-dependent phenomena in complex lasers *Phys. Rev.* A **92** 063829
[54] Casperson L W 1985 Spontaneous coherent pulsations in ring-laser oscillators: stability criteria *J. Opt. Soc. Am.* B **2** 993–7
[55] de Valcárcel G J, Roldán E and Prati F 1999 Risken-Nummedal-Graham-Haken instability in class-B lasers *Opt. Commun.* **163** 5–8
[56] Haken H 1986 *Laser Light Dynamics* 1st edn (North-Holland Publishing Company)
[57] Malik O 2017 Nonlinear and dynamical processes in complex lasers *PhD Thesis* Princeton University
[58] Chow W W, Schneider H C, Koch S W, Chang C-H, Chrostowski L and Chang-Hasnain C J 2002 Nonequilibrium model for semiconductor laser modulation response *IEEE J. Quantum Electron.* **38** 402–9
[59] Marskar R and Österberg U 2011 Multilevel Maxwell-Bloch simulations in inhomogeneously broadened media *Opt. Express* **19** 16784–96
[60] Jirauschek C, Riesch M and Tzenov P 2019 Optoelectronic device simulations based on macroscopic Maxwell-Bloch equations *Adv. Theory Simul.* **2** 1900018
[61] Haken H 1970 *Laser Theory* (Springer) pp 1–304
[62] Agrawal G 2013 *Nonlinear Fiber Optics* (Academic)
[63] Ge Li 2010 Steady-state *ab initio* laser theory and its applications in random and complex media *PhD Thesis* Yale University
[64] Cerjan A, Chong Y D and Douglas Stone A 2015 Steady-state *ab initio* laser theory for complex gain media *Opt. Express* **23** 6455–77
[65] Joannopoulos J D, Johnson S G, Winn J N and Meade R D 2011 *Photonic Crystals: Molding the Flow of Light - Second Edition* (Princeton University Press)
[66] Türeci H E, Douglas Stone A, Ge L, Rotter S and Tandy R J 2008 *Ab initio* self-consistent laser theory and random lasers *Nonlinearity* **22** C1–C18
[67] Fornberg B and Driscoll T A 1999 A fast spectral algorithm for nonlinear wave equations with linear dispersion *J. Comput. Phys.* **155** 456–67
[68] Hult J 2007 A fourth-order Runge-Kutta in the interaction picture method for simulating supercontinuum generation in optical fibers *J. Lightwave Technol.* **25** 3770–5
[69] Godey C, Balakireva I V, Coillet A and Chembo Y K 2014 Stability analysis of the spatiotemporal Lugiato-Lefever model for Kerr optical frequency combs in the anomalous and normal dispersion regimes *Phys. Rev.* A **89** 063814
[70] Gordon A *et al* 2008 Multimode regimes in quantum cascade lasers: from coherent instabilities to spatial hole burning *Phys. Rev.* A **77** 053804
[71] Meng B, Singleton M, Shahmohammadi M, Kapsalidis F, Wang R, Beck M and Faist J 2020 Mid-infrared frequency comb from a ring quantum cascade laser *Optica* **7** 162
[72] Kazakov D, Opačak N, Beiser M, Belyanin A, Schwarz B, Piccardo M and Capasso F 2021 Defect-engineered ring laser harmonic frequency combs *Optica* **8** 1277
[73] Micheletti P, Senica U, Forrer A, Cibella S, Torrioli G, Frankié M, Beck M, Faist Jôme and Scalari G 2023 Terahertz optical solitons from dispersion-compensated antenna-coupled planarized ring quantum cascade lasers *Sci. Adv.* **9** 24
[74] Narducci L M, Sadiky H, Lugiato L A and Abraham N B 1985 Experimentally accessible periodic pulsations of a single-mode homogeneously broadened laser (the Lorenz model) *Opt. Commun.* **55** 370–6
[75] Khan S A and Türeci H E 2017 Competing role of interactions in synchronisation of exciton-polariton condensates *New J. Phys.* **19** 105008